Particle Size and Dispersion Measurements

Gérard Bergeret, Pierre Gallezot

3.1.2
Particle Size and Dispersion Measurements

*Gérard Bergeret and Pierre Gallezot**

3.1.2.1 Definitions and Generalities

3.1.2.1.1 **Particles** In material sciences, ''particle'' is a general term for small solid objects of any size from the atomic scale (10^{-10} m) to the macroscopic scale (10^{-3} m); however, it often corresponds to the size range 10^{-9}–10^{-5} m as far as catalysts are concerned. The larger particles ($>10^{-6}$ m) are usually called grains (zeolites, carbons, Raney metals) and the smaller particles (<2 nm) are frequently called nanoparticles, aggregates (metals) or clusters (metals, oxides). The term crystallite describes a small single crystal; particles could be formed by one or more crystallites. In this chapter, particles corresponding to the active phases (metals, oxides, sulfides), rather than to the catalyst supports, will be considered and emphasis will be placed on metal particles.

---

* Corresponding author.

1

3.1.2.1.2 Particle Size Apart from molecular metal clusters (e.g. polynuclear metal carbonyls) or molecular oxide clusters (e.g. heteropolyanions), catalyst particles present a size distribution which can be very narrow, such as metal particles fitting in zeolite cages, or very broad, possibly with two or more maxima. Further complications arise because particles are usually not spherical and their shape is not homogeneous. A combination of two or more physical methods can in certain cases give an approximate description of both particle size and shape, particularly in favorable cases, as for plate-like particles. However, it is generally not possible to establish both the size and shape distribution so that in order to establish a size distribution and/or a mean size, particles are assumed to be spherical.

Let us consider a collection of n_i spherical particles of diameter d_i, of area A_i (or πd_i^2) and of volume V_i (or $\pi d_i^3/6$). Two types of size distribution are usually considered, namely the number distribution, which is a plot of n_i as a function of d_i, and the area distribution, which is a plot of $n_i d_i^2$ as a function of d_i. The latter gives more weight to the larger particles and therefore is more representative of the metal surface. A comparison between these two types of distribution is given in Section 3.1.2.5.4.

Two mean particle sizes are usually considered, the length-number mean diameter, $d_{LN} = \Sigma n_i d_i / \Sigma n_i$, and the volume-area mean diameter, $d_{VA} = \Sigma n_i d_i^3 / \Sigma n_i d_i^2$. The latter is the most useful parameter because it is related to the specific surface area (see Section 3.1.2.1.5) and therefore can be derived indirectly from surface area measurements by chemisorption (Section 3.1.2.2) or small-angle X-ray scattering (SAXS) (Section 3.1.2.4), as well as directly from granulometry measurements by electron microscopy (Section 3.1.2.5).

3.1.2.1.3 Nuclearity of Particles Figure 1 gives the total number of atoms as a function of particle size for spherical platinum particles. The continuous line was obtained by plotting the ratio of the particle volume ($\pi d^3/6$) to the volume v_m of a platinum atom in the bulk as a function of the particle diameter. Each point of the dotted line was calculated by a routine program which involved counting the atoms in a sphere of diameter d intercepting the three-dimensional array of atoms established from platinum crystal data. These curves, in excellent agreement since they are based on the same spherical model, indicate that the number of atoms increases very rapidly with increase in particle diameter.

More realistic particle models are obtained by considering regular polyhedra rather than spheres. Statistics of atoms in various polyhedra have been calculated by van Hardeveld and Hartog [1]. Figure 1 gives the number of atoms calculated for regular cubooctahedra [2]. For

a given diameter, it is easily seen that cubooctahedra contain fewer atoms than spheres.

3.1.2.1.4 Dispersion This term is mostly used for metal catalysts, although it could well be extended to other catalyst types. Let N_S be the total number of metal atoms present on the surface and N_T the total number of metal atoms (surface and bulk). The metal dispersion D is given by

$$D = \frac{N_S}{N_T}$$

The dispersion, i.e. the fraction of surface atoms, is usually between 0 and 1 (or 0 and 100%). Chemisorption measurements give direct measurement of the number of surface atoms (see Section 3.1.2.2) but, in the case of spherical particles, D can also be deduced using the relations between D and the specific surface area or the mean particle size d_{VA}, given in Section 3.1.2.1.5.

3.1.2.1.5 Relationships Between Particle Size, Surface Area and Dispersion For spherical particles, useful relationships between metal dispersion, surface area and mean particle diameter can be established by making assumptions on the nature of the crystal planes exposed on the metal surface [3–5]. Thus, assuming equal proportions of the three low-index planes (111), (100) and (110) on the polycrystalline surface of a face-centered cubic (fcc) metal, it is easy to calculate, from crystal data,

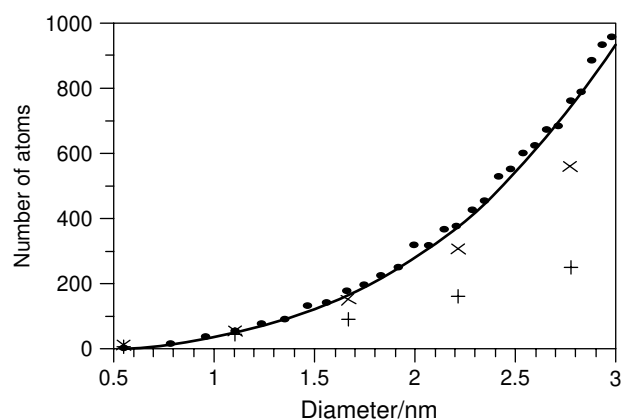**Fig. 1** Number of atoms in model platinum particles as a function of particle diameter d. The continuous curve is the ratio of $(\pi d^3/6)/v_m$ as a function of diameter (d = particle diameter, v_m = volume of a Pt atom in bulk platinum). ●, Total number of atoms encompassed in a sphere of diameter d; ×, total number of atoms in regular cubooctahedra; +, number of surface atoms in regular cubooctahedra.

the number of atoms per unit area in these planes and the mean number of atoms n_s. Table 1 gives a sample calculation for iridium.

The surface area a_m occupied by an atom m on a polycrystalline surface is $a_m = 1/n_s$. In the case of iridium this is $1/1.29 \times 10^{19} = 7.73 \times 10^{-20}$ m² (or 7.73 Å²). The volume v_m occupied by an atom m in the bulk of metal is given by

$$v_m = \frac{M}{\rho N_A}$$

where M is the atomic mass, ρ the mass density and N_A Avogadro's number (6.022×10^{23} mol^{-1}). In the case of iridium ($M = 192.2$ g mol^{-1}; $\rho = 22.42$ g cm^{-3}), $v_m = 14.24$ Å³.

Table 2 gives a list of n_s, a_m and v_m values for the most common metals used in catalysis.

The relationship between specific surface area (S_{sp}) and dispersion (D) is

$$S_{sp} = a_m \left(\frac{N_A}{M} \right) D \tag{1}$$

Thus, for iridium ($M = 192.2$; $a_m = 7.73 \times 10^{-20}$ m²), S_{sp} (m² g^{-1}) $= 242.2 D$.

The relationship between specific surface area (S_{sp}) and mean particle size (d_{VA}) is

$$S_{sp} = \frac{\sum n_i A_i}{\rho_i \sum n_i V_i}$$

Since $A_i = \pi d_i^2$ and $V_i = \pi d_i^3/6$, S_{sp} is given by

$$S_{sp} = \left(\frac{6}{\rho} \right) \frac{\sum n_i d_i^2}{\sum n_i d_i^3}$$

and, since $d_{VA} = \Sigma n_i d_i^3 / \Sigma n_i d_i^2$,

$$S_{sp} = \frac{6}{\rho d_{VA}} \tag{2}$$

With d_{VA} expressed in nanometers, ρ in g cm^{-3} and S_{sp} in m² g^{-1}, this becomes

$$S_{sp} = \frac{6000}{\rho d_{VA}}$$

The relationship between metal dispersion (D) and mean particle size (d_{VA}) is

$$d_{VA} = 6 \left(\frac{\sum n_i V_i}{\sum n_i A_i} \right) = 6 \left(\frac{v_m N_T}{a_m N_S} \right)$$

Since $N_S/N_T = D$, then

$$D = 6 \frac{(v_m/a_m)}{d_{VA}} \tag{3}$$

The usefulness of Eqs. (2) and (3) is illustrated in Figs. 2 and 3, which show plots of D and S_{sp}, respectively, as a function of the mean size, d_{VA}, for nickel, palladium and platinum. Table 2 gives the values of S_{sp} and D corresponding to $d_{VA} = 5$ nm for various metals.
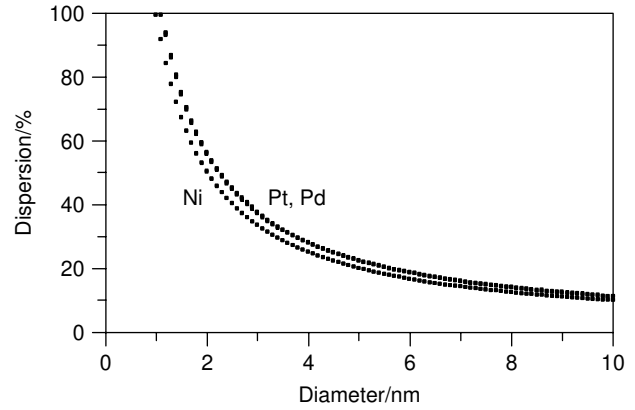
Fig. 2 Plot of dispersion D as a function of mean diameter d_{VA} for nickel, palladium and platinum.
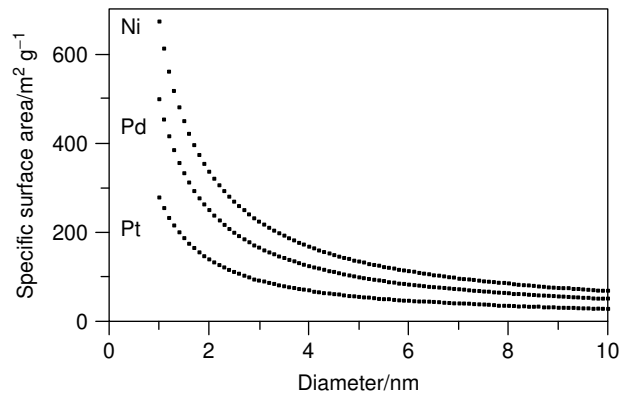
Fig. 3 Plot of specific surface area S_{sp} as a function of mean diameter d_{VA} for nickel, palladium and platinum.

Tab. 1 Number of atoms per unit area in the three low-index planes of iridium (fcc structure with unit cell constant $a = 3.8394$ Å) and mean number n_S for equal proportions of planes on the surface of particles

Plane	Surface cell	Area	Atoms per cell	Atoms per $10^{-19} m^2$
(111)	Triangular	$(a^2\sqrt{3})/2$	2	1.57
(100)	Square	a^2	2	1.36
(110)	Rectangular	$a^2\sqrt{2}$	2	0.96
				$n_S = 1.29 \times 10^{19}$

Tab. 2 Useful data on metals and relation between dispersion, mean diameter and specific surface corresponding to a diameter $d_{VA} = 5$ nm[a]

Metal	Structure	n_s	$a_m/Å^2$	$M/g\ mol^{-1}$	$\rho/g\ cm^{-3}$	$v_m/Å^3$	D	$S_{sp}/m^2\ g^{-1}$
Ag	fcc	1.14	8.75	107.87	10.50	17.06	0.23	114.3
Au	fcc	1.15	8.75	196.97	19.31	16.94	0.23	62.1
Co	fcc	1.52	6.59	58.93	8.90	11.00	0.20	134.8
Co	hcp	1.84	5.43	58.93	8.90	11.00	0.24	134.8
Cr	bcc	1.62	6.16	52.00	7.20	11.99	0.23	166.7
Cu	fcc	1.46	6.85	63.55	8.92	11.83	0.21	134.5
Fe	bcc	1.64	6.09	55.85	7.86	11.80	0.23	152.7
Ir	fcc	1.29	7.73	192.22	22.42	14.24	0.22	53.5
Mo	bcc	1.36	7.34	95.94	10.20	15.62	0.26	117.6
Ni	fcc	1.54	6.51	58.69	8.90	10.95	0.20	134.8
Os	hcp	1.54	6.47	190.20	22.48	14.05	0.26	53.4
Pd	fcc	1.26	7.93	106.42	12.02	14.70	0.22	99.8
Pt	fcc	1.24	8.07	195.08	21.45	15.10	0.22	55.9
Re	hcp	1.52	6.60	186.21	20.53	15.06	0.27	58.5
Rh	fcc	1.32	7.58	102.91	12.40	13.78	0.22	96.8
Ru	hcp	1.57	6.35	101.07	12.30	13.65	0.26	97.6
W	bcc	1.35	7.42	183.85	19.32	15.78	0.26	62.0

[a] n_S = number of surface atoms per 10^{-19} m^2 calculated using the following proportions of low index planes: fcc (111) : (100) : (110) = 1 : 1 : 1; bcc (110) : (100) : (211) = 1 : 1 : 2; hcp (001); a_m = area occupied by a surface atom; M = atomic mass; ρ = mass density; v_m = volume occupied by an atom in bulk metal; D = metallic dispersion corresponding to $d_{VA} = 5$ nm; S_{sp} = specific surface area (m^2 g^{-1}) corresponding to $d_{VA} = 5$ nm.

It should be noted that for very small particles, geometric models assuming a given particle morphology (cubooctahedron, truncated octahedron or tetrahedron) rather than spheres should be considered. For instance, a collection of 40 atoms of 1.3 nm diameter as a truncated tetrahedron would have almost the same dispersion (36/40 = 0.90) as 13 atoms of 0.83 nm diameter arranged as a cubooctahedron (12/13 = 0.92). This indicates that Eqs. (1)–(3) should not be used for particles smaller than ca. 1.2 nm.

3.1.2.1.6 **Methods of Particle Size Measurement** Particle size can be measured by chemical and physical methods. Chemical methods are based on measurements of the amount of gas chemisorbed on the surface of particles (Section 3.1.2.2). Provided that some assumptions are made on the stoichiometry of adsorption and on the nature of atomic planes exposed on the surface, the surface area and the particle size can be obtained using Eqs. (4) and (5) given below in Section 3.1.2.2.2A. This technique is limited to metals but it is widely used since it does not require any expensive equipment or special skills.

As far as physical techniques are concerned, emphasis will be placed on electron microscopy, which is the most powerful technique for particle size measurements (Section 3.1.2.5). Indeed, particles whose sizes span from the atomic to the macroscopic scale can be directly observed and measured on catalyst images. Techniques based on X-ray diffraction such as line broadening analysis (LBA) and small-angle X-ray scattering (SAXS) are also useful methods since they lead to both mean sizes and size distributions (Sections 3.1.2.3 and 3.1.2.4, respectively). The first method probes the crystallite sizes, whereas SAXS probes the particle sizes; therefore, these techniques are complementary since a particle can be polycrystalline. However, except for simplified LBA (using linewidths at half-height), they are not in widespread use because they require special apparatus and rather cumbersome calculations and therefore are carried out only by a few specialists. Similar comments hold for particle size measurements by magnetic methods. These techniques are discussed in less detail than electron microscopy (Section 3.1.2.6).

3.1.2.2 **Particle Size Measurements by Gas Chemisorption**

3.1.2.2.1 **Introduction and Principles** Selective chemisorption (i.e. formation of an irreversibly adsorbed monolayer) is the most frequently used technique for characterizing metallic catalysts. The measurement of the quantity of a gas adsorbed selectively on the metal at monolayer coverage gives the metal surface area and the metal dispersion, if the stoichiometry of the reaction of chemisorption is known. Basic information

can be found in the classical monograph by Anderson [6]. Hydrogen chemisorption as a probe for metal dispersion has been reviewed in detail [7–9]. Bartholomew [9] presented recommendations for the correct use of this characterization method. A British Standard [10] described methods for the determination of metal surface area using gas adsorption with specific recommendations for Ni, Pd, Pt and Cu. Recently, Anderson et al. [11] reviewed selective chemisorption methods with emphasis on Pt, Pd, Rh, Ni and Cu.

3.1.2.2.2 **Gas Adsorption–Desorption Methods** Measurement of the gas uptake has been carried out by static methods, such as volumetry and gravimetry, and also dynamic methods based on gas thermal conductivity, such as continuous flow and pulse adsorption methods. Evaluation of the metal surface area by desorption methods, such as temperature-programmed desorption coupled to mass spectrometry, is of increasing use.

A   Static Methods   Many studies have been performed by static volumetry. Schematically, the apparatus consists of a gas dosing device, a pressure gauge, a pumping system, a cell and an oven for the sample. Typical unit descriptions can be found in the literature [12, 13]. The catalyst, previously pretreated and evacuated, is contacted by a known quantity of the adsorbate gas. The amount of adsorbed gas is determined by measuring the pressure after a certain delay (10–60 min) for reaching the adsorption equilibrium, the volume of the system (dead space) being known by a preliminary calibration. Successive doses of gas allow the determination of the amount of adsorbed gas versus the equilibrium pressure, i.e. the adsorption isotherm. In the gravimetric method, the amount of adsorbed gas is measured by weighing the sample with an electrobalance. The adsorption is often carried out at room temperature. The pressure range depends on the nature of the metal but more than one order of magnitude is advisable. Commercial automatic equipment is available.

To evaluate the chemisorbed monolayer uptake v_m (saturation of the metal surface), a common practice is to back-extrapolate the straight portion of the isotherm to zero pressure. This procedure becomes ambiguous if the isotherm does not present a horizontal region, but only a linear or approximately linear region. Figure 4 shows the isotherms for the adsorption of CO on EUROPT-1 Pt/SiO$_2$ catalyst from different laboratories over two ranges of pressure [14]. High surface coverage seems to be achieved at an equilibrium pressure of 0.2 kPa. However, there is a linear increase in the adsorbed volume with increasing pressure. Extrapolations of the isotherms to nominally zero pressure, as shown by the dashed line in Fig. 4,
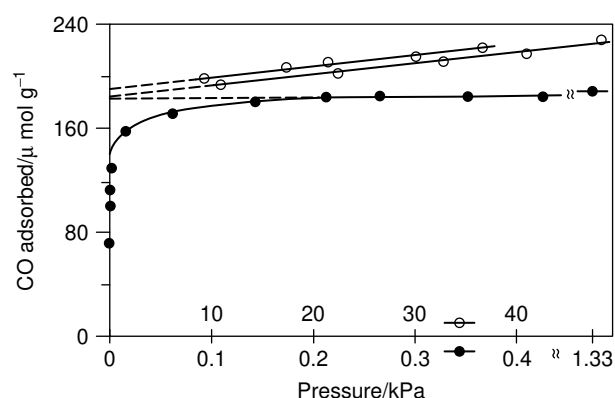

Fig. 4 Isotherms for the adsorption of CO on EUROPT-1 Pt/SiO$_2$ catalyst at room temperature from different laboratories for a pressure range 0–1.33 kPa (solid circles) and 10–50 kPa (open circles). (Adapted from Ref. [14].)

provide values of 185–198 µmol CO g^{-1} for the extent of monolayer adsorption.

From the volume of chemisorbed gas required to form the monolayer v_m, the specific metal surface area A is given by

$$A = \frac{v_m}{22414} N_A \, n \, \frac{1}{m} \, a_m \, \frac{100}{wt} \ (\text{m}^2 \text{ g}^{-1} \text{ metal}) \qquad (4)$$

where v_m is expressed in cm^3 (STP), N_A is Avogadro's number $(6.022 \times 10^{23} \text{ mol}^{-1})$, n the chemisorption stoichiometry, m the mass of the sample (g), a_m the surface area (m^2) occupied by a metal atom and wt (%) the metal loading. The chemisorption stoichiometry represents the average number of surface metal atoms associated with the adsorption of each gas molecule at monolayer coverage [6].

The metal dispersion is directly obtained by

$$D = \frac{v_m n}{22414 m} \Big/ \frac{wt}{100 M} \qquad (5)$$

where M is the atomic mass of metal.

There are isotherms where the foregoing procedure is not at all practical, as shown in Fig. 5 [15]; see also, for instance, the study of H$_2$ chemisorption on EUROPT-1 Pt/SiO$_2$ catalyst [16]. The equilibrium coverage increases very significantly with increase in the adsorption pressure and saturation corresponding to the monolayer is not reached. Therefore, the volume corresponding to the monolayer v_m is generally obtained by empirically fitting the adsorbed volume to the adsorption isotherm of a given type. The Langmuir isotherm for dissociative adsorption:

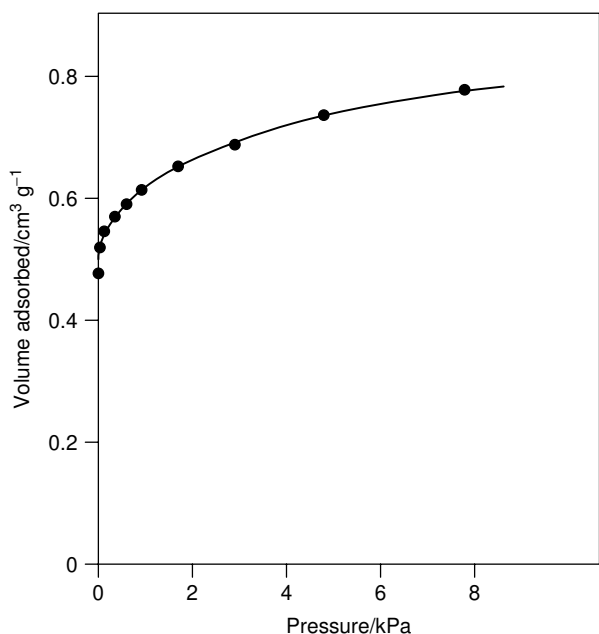$$v = \frac{v_m b p^{1/2}}{1 + b p^{1/2}}$$

5

Fig. 5 Hydrogen adsorption isotherm at 333 K on a 2% Pt/Al$_2$O$_3$ catalyst. (Adapted from Ref. [15].)

Fig. 6 Isotherms of H$_2$ adsorption on 0.5% Pt on γ-alumina at 303 K: (a) total amount of adsorbed H$_2$; (b) amount of reversibly adsorbed H$_2$ after evacuation at room temperature. (Adapted from Ref. [17].)

is often used [6, 15]. Plots of either $1/v$ against $1/p^{1/2}$ or $p^{1/2}/v$ against $p^{1/2}$ are used to evaluate v_m.

Depending on the nature of metals and gases and operating conditions (temperature, pressure, measurement method), strongly and weakly bound species may coexist on the metal surface and the chemisorption may be in part reversible. Reversible chemisorption on the support is also possible. The terms reversibility and irreversibility have operational meaning only. Bartholomew [9] examined the problem of the reversibility of hydrogen adsorption in connection with metal dispersion determination.

Figure 6 shows the isotherms of hydrogen adsorption on a Pt/Al$_2$O$_3$ catalyst [17]. The upper and lower isotherms represent the total (H_T) and reversible (H_{rev}) adsorption of hydrogen, respectively. The quantity of reversibly adsorbed H$_2$ is determined from readsorption measurements, after evacuation of the gas at the same temperature. The irreversible hydrogen adsorption (H_{irr}) is given by the difference $H_T - H_{rev}$. The question as to whether the reversible hydrogen adsorption is attributable to the support or to the metal is controversial. In the present case, it was considered that the reversibly adsorbed hydrogen was associated with the metal surface and that H_T was more suitable than $H_T - H_{rev}$ for estimation of the metal surface area, in agreement with results from microscopy. However, dispersions higher than 100% could be obtained when platinum is highly dispersed, because the adsorption stoichiometry H/Pt$_S$ may be greater than unity due to multiple adsorption of hydrogen on certain Pt
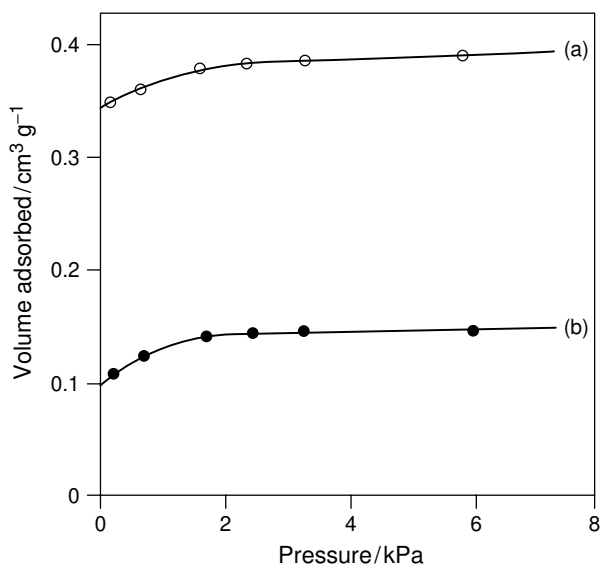
sites. Therefore, many authors prefer to use irreversibly adsorbed hydrogen with a stoichiometry value of 1.0.

B Dynamic Methods   Flow techniques are faster and more convenient than static methods since they do not require vacuum systems, but they are less adapted to the determination of the adsorption isotherm. In the continuous flow technique (frontal chromatography or, more precisely, frontal sorption method), the pretreated catalyst is flushed by an inert gas (e.g. Ar) at a sufficiently high temperature to desorb all the adsorbed molecules. Then, after cooling to the adsorption temperature, the flow is switched to the adsorbate gas (e.g. 2% H$_2$−Ar) until the detector (thermal conductivity cell) downstream shows a constant gas phase composition. After purging, the reactive gas is switched on again to evaluate the dead volume and the possible reversible adsorption. The gas uptake by the metal particles is determined from the difference in the two quantities. In the pulse technique (pulse chromatography or pulse sorption method), the adsorbate gas is injected as successive small pulses of known volume into the flow of the inert gas. The irreversibly chemisorbed gas quantity is obtained from the number of pulses consumed [18].

C Desorption Methods   Temperature-programmed desorption (TPD) of adsorbed gas from catalysts has

become a very common technique for catalyst characterization [7, 8, 19], since it gives much more information than the methods described previously. The information collected from TPD studies is (i) the type and amount of the different forms of adsorbed species, (ii) the bond energies between adsorbate and surface and possibly (iii) the type of bonding of the adsorbed species on the catalyst surface [8]. However, the determination of the amount of chemisorbed gas is not always very accurate because of various experimental considerations (diffusion, readsorption).

Experimentally, the pretreated catalyst is contacted by the adsorptive gas. After the elimination of excess gas, the catalyst is heated with a linear ramp of temperature and desorbed products are analyzed with a gas thermal conductivity detector or, preferably, with a mass spectrometer. The desorption rate of the adsorbed gas increases, passes through a maximum and drops back to zero as the surface is depleted of adsorbate. The area of the desorption profile (amount of desorbed gas as a function of temperature) provides the amount of initially adsorbed gasw.

3.1.2.2.3 Choice of Adsorbate Gases

Ideally, for a given catalyst, the gas (and the operating conditions) should be chosen to minimize adsorption on the support and to have an irreversible (or weakly reversible) chemisorption on the metal. This can be established from TPD data. Among the gases mentioned in the literature (CO, H_2, O_2, N_2O, NO, N_2, H_2S, CS_2, C_6H_6, etc.), only the first three are in common use, the others being dedicated to specific applications. The recurring problem of selective chemisorption is choosing the true adsorption stoichiometry for a given gas−metal system. The chemisorption stoichiometries for catalytically important metals are listed in Table 6 of Ref. [20] and in Ref. [9] for hydrogen on supported noble metals. To summarize these data, the CO : metal stoichiometry varies from 1 to 2 (see below); the value of H : metal = 1.0 has been verified for Pt, Pd, Rh, Ru, Ir and Ni supported on a variety of carriers. Some exceptions have been reported for supported catalysts of very high dispersion where H : metal >1 and for zeolite supported catalysts (see Section 3.1.2.2.4). The O : metal stoichiometry is 1.0 but the possible formation of metal oxides with variable stoichiometries and of bulk metal oxides may be the cause of difficulties. The main application of oxygen adsorption measurements is hydrogen−oxygen titration (see Section 3.1.2.2.4). Chemisorption on metal powders of known BET area and physical techniques such as electron microscopy, X-ray diffraction line broadening or small-angle X-ray scattering (see Sections 3.1.2.3−3.1.2.5) may be used to confirm the various stoichiometries proposed.

The chemisorption of carbon monoxide has often been used for metal surface area measurements. A difficulty encountered is that carbon monoxide is chemisorbed in various forms on metals such as iron, nickel, ruthenium, palladium, rhodium and platinum. Carbon monoxide can be chemisorbed dissociatively (CO : metal $\geq$ 2) or associatively in a linear ($n = 1$), bridged ($n = 2$) and capped ($n = 3$) form; the relative proportions of the various forms are not only temperature and pressure but also metal particle-size dependent [7]. A CO : metal stoichiometry of 1 : 1 has commonly been used, for example on Pt [14], although bridged carbon monoxide coexists with the predominant linear form. On palladium, the proportion of the bridged form is larger and varies with the dispersion, but nevertheless numerous authors used a CO : Pd stoichiometry of 1 : 1 [21−23]. In recent well-documented studies [24−26], an average value close to 2 was found valid whatever the nature of the support or the Pd dispersion, provided that measurements are performed using a pulse flow technique [26]. Beck et al. [27], taking into account that CO is chemisorbed partly in linear and partly in bridged form, assumed an average CO : Pd stoichiometry of 1.5. This value is also suggested in a British Standard [10]. Another difficulty is the formation of carbonyls where two or more CO molecules are bonded to a metal atom. Metal carbonyls can be volatile, e.g. in the case of nickel or rhodium. Their formation is easier if the metal is in a finely divided state. Thus, it was demonstrated [28] that CO molecules can extract atoms from 1-nm rhodium aggregates that were completely disaggregated. CO chemisorption is better suited than H_2 chemisorption in the case of significant adsorption of H_2 on the support (e.g. carbon supports).

The metallic area accessible to gases can be also deduced from Fourier transform infrared (FTIR) spectroscopy of linearly bonded CO [29]. By using this technique, it is possible to discriminate the CO adsorption on the metal from the adsorption on the support. This technique is well adapted to easily reducible supports such as TiO_2, CeO_2 [30, 31] and ZrO_2 [31], which give rise to the so-called strong metal−support interaction (SMSI) effect, to samples exhibiting hydrogen spillover and to supports able to adsorb the probe molecules.

In cases where a metal presents a very low reactivity towards H_2 or CO and an excessively strong interaction with oxygen, such as for Cu and Ag, the adsorptive decomposition of nitrous oxide (N_2O) can be used. This technique has been used to determine ruthenium dispersion [32].

3.1.2.2.4 Hydrogen Chemisorption; Hydrogen−Oxygen Titration

Generally, hydrogen adsorbs dissociatively on metals according to

$$H_2 + 2M_s \longrightarrow 2M_s-H$$
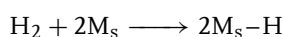
where M_s represents a metal surface atom, with a stoichiometry of one hydrogen atom per metal surface atom [$n = 2$ in Eqs. (4) and (5)]. This value of $H:M_s = 1$ is well established for a number of supported Group VIII metals [20, 33]. The case of supported platinum was detailed by O'Rear et al. [34] and was reviewed recently by Anderson et al. [11]. Data compiled by Bartholomew [9] show $H:M_s$ values of 1.0–1.2 for Pt, Pd, Rh, Ru and Ir on various supports. Standardized chemisorption procedures for measuring metal dispersion have been published by the American Society for Testing and Materials (originally published in 1980; current edition revised in 2003) [35] and the Japan Catalysis Society [36]; the two methods concern H_2 chemisorption on Pt/alumina catalysts measured by a volumetric method. A British Standard [10] proposes H_2, O_2 and CO chemisorption procedures on Pt, Pd and Ni. The main features of these procedures, which could be applied to other gas–metal systems after adaptation, are given below. Pretreatment consists of (i) heating in air or oxygen up to 623–723 K to ensure removal of adsorbed hydrocarbons from the catalyst surface due to ambient contamination, (ii) evacuation at this temperature and cooling under vacuum, (iii) heating in H_2 from room temperature to 623–723 K to reduce the catalyst and (iv) evacuation at 698 K and cooling under vacuum. The uptake of H_2 is measured at room temperature after an equilibrium delay of 30–60 min for each dose of gas.

Hydrogen–oxygen titration was introduced in 1965 by Benson and Boudart [37] for alumina-supported platinum catalysts as a sensitive, simple and convenient method. The proposed reactions are as follows:

$$Pt_s + \frac{1}{2}H_2 \longrightarrow Pt_s\text{–}H \quad \text{hydrogen chemisorption (HC)}$$

$$Pt_s + \frac{1}{2}O_2 \longrightarrow Pt_s\text{–}O \quad \text{oxygen chemisorption (OC)}$$

$$Pt_s\text{–}O + \frac{3}{2}H_2 \longrightarrow Pt_s\text{–}H + H_2O \quad \text{hydrogen titration}$$
of oxygen-covered surface (HT)

$$2Pt_s\text{–}H + \frac{3}{2}O_2 \longrightarrow 2Pt_s\text{–}O + H_2O \quad \text{oxygen titration}$$
of hydrogen-covered surface (OT)
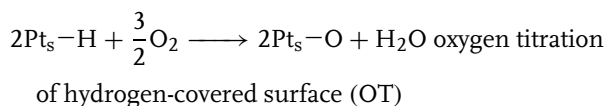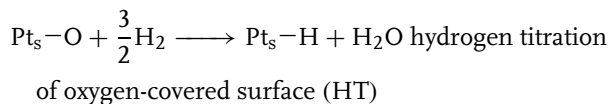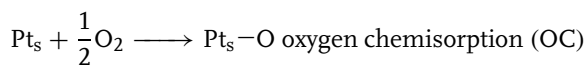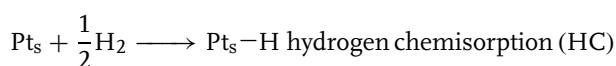
with a stoichiometry $HC:OC:HT:OT$ of $1:1:3:3$. Therefore, the sensitivity of H_2–O_2 titration is three times greater than for direct H_2 or O_2 chemisorption.

After more than 20 years of development of this method [8, 9], it clearly appears that the results of the titration (i.e. stoichiometry of $1:1:3:3$) depend strongly on the pretreatment of the sample and on the procedure of the titration. The careful work of O'Rear et al. [34] in 1990 ended the discussions and recommended a procedure for the H_2–O_2 titration of supported platinum catalysts; this procedure is generally accepted. The hydrogen–oxygen titration of palladium was recently re-examined by Prelazzi et al. [38].

Various effects can modify the $H:Ms = 1.0$ stoichiometry of hydrogen chemisorption:

(i) Spillover of H atoms (Chapter 5.3.2) from the metal to the support, leading to $H:M_s$ values higher than 1.0. This is often a slow process favored by the presence of water and impurities (chlorine, sulfur, carbon). It depends on the nature of the support, e.g. it is large on carbon supports (for the factors influencing spillover, see Refs. [9] and [39]).

(ii) SMSI effect (Section 3.2.5.1). The decoration of the metal by (partially) reduced support species decreases the H_2 uptake. This mechanism depends on the nature of the support (oxides from Groups IIIB–VB) and is increased by excessively prolonged heat treatment and reduction at high temperatures. These effects can be reversed through cycling in O_2 and H_2. In some cases of reduction at high temperatures, even intermetallic compounds (Ni–Si, Pd–Si, Pt–Al) may be formed.

(iii) Hydrogen absorption occurs for a number of metals and leads to the formation of either a true solid solution or a hydride. Thus, for palladium an appropriate procedure is needed to avoid bulk hydride formation [40, 41]. At 373 K, the β-phase palladium hydride does not begin to form until the hydrogen pressure reaches 46.7 kPa. Therefore, H_2–O_2 titration performed at 373 K gives correct results in agreement with X-ray diffraction line broadening and chemisorption of oxygen or carbon monoxide [41].

(iv) The presence of contaminants – residues of preparation (Cl, ligands, solvent) or species coming from the support (Cl, S) or the gas phase (impurities of reactants, H_2O, S, C, residues of reaction CH_x) – can also alter the gas uptake. Small amounts of metallic impurities can segregate from the bulk of the metal particles to the surface under the influence of temperature and modify the chemisorption.

(v) The support ionicity can modify strongly the hydrogen coverage on metal particles, as shown by a recent study on zeolite Y-supported Pt particles [42].

These perturbing effects for the chemisorption have been studied extensively for hydrogen, but they can be largely transposed, particularly contaminant effects, to other adsorbates.

3.1.2.2.5 Conclusion and Recommendations Ideally, for a given catalyst, the gas and the operating conditions should be chosen to minimize the adsorption on the support and to have an irreversible (or weakly reversible) chemisorption on the metal. This can be established from TPD data or IR spectroscopy. Some methods for determining the gas uptake, such as thermodesorption methods and pulse methods, measure only irreversible adsorption. A fresh catalyst should be homogenized by a few H_2-O_2 cycles at ambient temperature to obtain reproducible gas uptake [8, 43]. Generally, prolonged reductions or evacuations at high temperatures should be avoided, insofar as they favor H_2 spillover, SMSI effects and various contaminations.

In conclusion, when the operating conditions are selected, chemisorption is a convenient method for routine dispersion measurements. However, one should keep in mind that the dispersion and particle size determination from the gas uptake involves many assumptions and depends on the conditions of catalyst treatment. In fact, chemisorption probes the exposed surface area, i.e. the surface directly related to catalyst activity. A good policy is to use either the chemisorption of two or even three different adsorbates (e.g. H_2, O_2, CO [44]) or to use chemisorption and titration in order to check the consistency of the measurements [9] and to minimize the risk of artifacts (spillover, SMSI, contaminants, reversible adsorption). In fact, chemisorption measurements employed to determine metal particle sizes are more and more frequently associated with electron microscopy [44] and/or X-ray diffraction measurements [21].

3.1.2.3 X-Ray Diffraction Line Broadening Analysis

3.1.2.3.1 Introduction X-ray diffraction line broadening analysis (LBA) is widely used for characterizing the particle size of catalysts. However, the breadth of an X-ray reflection on the lattice planes of crystallites (small single crystals) depends on the characteristics of the crystallites (size and defects in the lattice) and instrumental factors. The analysis of the diffraction line involves the determination of these three factors.

LBA can be carried out either at an elementary level or a more sophisticated level. At the simplest level, the application of the Scherrer equation leads to an estimate of the mean crystallite size. At a more elaborate level, the complete line profile analysis with Fourier methods allows the determination of crystallite size distributions and crystallite lattice strains. The application of LBA to catalysts was described by Gallezot [45] and Matyi et al. [46]. These classical methods continue to be used but progress in data analysis has allowed the emergence of the whole powder pattern fitting methods derived from the Rietveld refinement. They are applicable to X-ray patterns with overlapping reflections, unlike earlier LBA methods, as underlined by Langford [47]. Two recent books deal with the analysis of the microstructure of materials by diffraction, with emphasis on the new methods [48, 49].

3.1.2.3.2 Elementary Line Broadening Analysis: the Scherrer Equation The elementary analysis of the broadening assumes that the lattice defects of the particles (microstrains or stacking faults) are negligible. Moreover, the instrumental broadening is calculated in a simplified way. Consider an X-ray reflection on N lattice planes of spacing d_{hkl}. Scherrer [50] showed that the thickness of the crystallite, $L = N d_{hkl}$, in the direction perpendicular to the diffracting planes (hkl) can be obtained from the breadth β of the diffraction profile using the relationship

$$L_{hkl} = \frac{k\lambda}{\beta \cos \theta_0}$$

where k is a constant (see below), λ is the wavelength of the X-radiation employed, β is expressed in radians and θ_0 is the angular position of the peak maximum. The size of the crystallites is thus inversely proportional to the breadth of the diffraction line.

Two definitions of β are used: the full width at half-maximum intensity (FWHM), often written as $\beta_{1/2}$, and the integral breadth β_i (total area under the line profile divided by the line intensity at maximum), which is the width of an equivalent rectangle whose height is equal to the peak maximum and whose area is equal to the integrated area under the peak. The latter definition is the most fundamental one and, in the general case of non-identical crystallites (i.e. in all practical cases), it was demonstrated [51] that the size L obtained from β_i is the volume-weighted average size:

$$L = \langle D_v \rangle = \left(\frac{1}{V} \right) \int V_D D \, dD$$

where V is the volume of the sample and V_D the volume of crystallites for which the height normal to the reflecting lattice planes lies between D and $D + dD$. If one considers a collection of n_i spherical particles of diameter d_i, the Scherrer equation with β_i measures the volume-weighted average diameter $d_v = \Sigma n_i d_i^4 / \Sigma n_i d_i^3$. Conversely, L measured from $\beta_{1/2}$ has no clear physical meaning. Moreover, the smaller crystallites, which contribute mainly to the wings of the line profile, are scarcely taken into account using $\beta_{1/2}$ and L could be greatly overestimated. Therefore, it is highly recommended to take the integral linewidth β_i instead of $\beta_{1/2}$, which is now very easy by using the software package supplied with modern automated powder diffractometers.

The constant k (also called shape factor) depends on the definitions of crystallite size and broadening (β_i or

$\beta_{1/2}$), the shape of the crystallites and the reflection being examined. The value of k could be adjusted for different (hkl) reflections and crystallite shapes in the case of crystallites identical in shape and dimensions [52]. However, this is of no practical use as far as catalysts are concerned and, in view of the approximations involved in the elementary analysis of the broadening, the value of k should be taken as unity (0.9 when $\beta_{1/2}$ is used).

The Scherrer equation assumed that a small crystallite size is the sole source of broadening of the diffraction profile. In fact, there is always a broadening due to the various instrumental factors such as slit widths, sample size, penetration of the X-ray beam into the specimen, imperfect focusing or misalignment of the diffractometer. The separation of the $K\alpha_1 - K\alpha_2$ doublet is carried out easily and satisfactorily using the computer programs integrated with the difractometers. The other instrumental factors are estimated from the diffraction profile of a standard sample giving a reflection line near θ_0 and containing crystallites large enough (i.e. ca. $0.2-2$ μm) and free from lattice distortion (metal, silicon, quartz, α-Al_2O_3 or LaB_6 powder, etc.). If both experimental and reference lines exhibit Gaussian profiles, the true peak breadth is given by the Warren equation [53]:

$$\beta^2 = \beta^2_{observed} - \beta^2_{reference}$$

Other corrections have been proposed depending on the shape of the diffracted profile [43] but, for supported catalysts, it is the Warren correction which experimentally gives the better results.

3.1.2.3.3 Complete Line Profile Analysis: the Warren–Averbach Method

The complete line profile analysis takes into account all the information available in a diffracted peak (shape as opposed to the width β) and allows a precise correction for the instrumental broadening and the effects of strain. Therefore, not only a mean particle size, but also the distribution of the particle size can be determined. This complete analysis, generally known as the Warren–Averbach method [54], is based on the representation of the diffracted intensity by the sum of the sine and cosine terms of a Fourier series. A detailed description of the method can be found in the advanced textbook on X-ray powder diffraction by Warren [55]. A recent update is given in Ref. [48].

The first step is the correction for the effects of instrumental broadening. The observed broadened diffraction profile described by the function $h(x)$ is a convolution of the true sample peak $f(y)$ with the instrumental broadening $g(z)$ which is obtained with a reference sample containing strain-free large crystallites:

$$h(x) = \int f(x-z)g(z)\,dz$$

The Stokes method [55, 56] permits extraction of the pure line profile $f(y)$ from the Fourier transform of $h(x)$ and $g(z)$ (i.e. the sine and cosine Fourier coefficients). Independently of the Fourier method, direct analytical methods, effective for unfolding the diffraction profile, have been reported (see, for instance, Ref. [57]).

The second step is the separation between size and strain broadening. The Stokes-corrected cosine coefficients A_L, from an (hkl) diffraction profile, can be decomposed into two terms: a size coefficient A_L^S and a distortion coefficient A_L^D, such that $A_L = A_L^S A_L^D$, where $L = n(\lambda/2)/(\sin\theta_{max} - \sin\theta_{min})$ and where n is the harmonic number, λ the wavelength and $2\theta_{max} - 2\theta_{min}$ the interval of the Fourier analysis. The distortion coefficient A_L^D is dependent on the order of the diffraction line [namely (222) vs. (111)], whereas the size coefficient A_L^S is independent of peak order. The size and distortion coefficient can be separated by the Warren–Averbach method [54], using two lines corresponding to multiple reflection orders. This method allows the determination of A_L^S and of the mean square strain. In the case for which it is difficult to make satisfactory intensity measurements on the higher order reflections (supported metal catalysts), Ganesan et al. [58] described an original method for determining the coefficients A_L^S and the mean square strain from the analysis of a single line profile.

The third step is the derivation of size parameters from the A_L^S coefficients [54, 59]. A surface-weighted mean diameter $\langle D_s \rangle$, perpendicular to the (hkl) planes under consideration, is obtained from the first derivative of A_L^S at $L = 0$. In practice, the intercept of the initial slope of the A_L^S versus L curve on the L axis gives $\langle D_s \rangle$ directly. It should be noticed that the mean particle sizes measured by the Fourier analysis, $\langle D_s \rangle$, and by the Scherrer equation, L, are different [60]. If one considers a collection of n_i spherical particles of diameter d_i, $\langle D_s \rangle$ corresponds to the volume–area mean diameter $d_{VA} = \Sigma n_i d_i^3 / \Sigma n_i d_i^2$.

A volume-weighted size distribution can be obtained from the second derivative of the Fourier coefficients A_L^S. On the basis of this crystallite size distribution, a volume-weighted mean diameter $\langle D_V \rangle$ can be calculated, which is equivalent to that obtained from the Scherrer equation. The crystallite diameter distribution function can also be extracted directly from the pure diffraction profile with optimization analytical methods [61].

3.1.2.3.4 Examples of Application of Classical LBA to Catalysts

Although not recent, the study of Pt/SiO_2 and Pd/C catalysts by Smith [60] is a good illustration of LBA on typical line profiles. The line profile of Pt/SiO_2 (Fig. 7a) is broad and flat; it corresponds to a narrow size

distribution, whereas that of Pd/C (Fig. 7b) is tall with extended wings and corresponds to a wide distribution of crystallite sizes. Table 3 gives the value of $\langle D_s \rangle$ obtained from the complete Fourier analysis compared with D_i and $D_{1/2}$ determined with the Scherrer equation from the integral linewidth β_i and from the linewidth at half-maximum $\beta_{1/2}$, respectively. The three mean diameters compare well when there is a narrow size distribution (Pt/SiO$_2$), but the Scherrer equation, particularly with the linewidth at half-maximum $\beta_{1/2}$ applied to the Pd/C profile, greatly overestimates the mean size because the smaller crystallites contributing to the tails of the profile are not taken into account.

A very complete study of the platinum particles on silica has been achieved by Sashital et al. [62]. In spite of the low metal concentration (1–2 wt.%), they derived crystallite size distributions in various directions, mean diameters and mean square strains from the X-ray pattern. The excellent agreement between the dispersion determined by chemisorption and from the surface-weighted mean diameters indicated that the particles are not polycrystalline. Furthermore, it was shown that the root mean square amplitudes of vibration of the platinum atoms increased with particle dispersion. A correlation between these atom displacements and the catalytic activity has been reported [63].
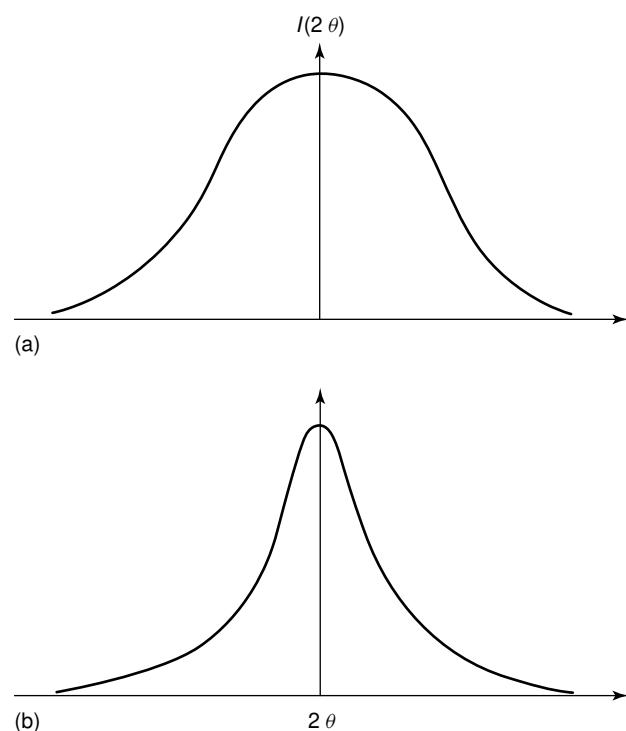

$I(2\theta)$

(a)

(b)

2θ

Fig. 7 Line profiles: (a) Pt/SiO$_2$ catalyst with a narrow distribution of crystallite sizes; (b) Pd/carbon catalyst with a wide distribution of crystallite sizes. (Adapted from Ref. [60].)

Tab. 3 Mean crystallite size (nm) from LBA [60]

Catalyst	$\langle D_s \rangle$	D_i	$D_{1/2}$
Pt/silica	5.3	6.0	5.9
Pd/carbon	4.3	7.2	13.0

Fourier single profile analysis is particularly useful in the case of supported metal catalysts where, owing to the difficulty of making satisfactory intensity measurements on the higher order reflections, it is very hard, if not impossible, to obtain the two orders of an (*hkl*) profile required for the Warren–Averbach method. The sintering of supported NiO was studied by Ganesan et al. [58] using the analysis of a single diffraction profile to obtain the particle size distribution function and the lattice strains. The single profile method was also used to investigate the sintering of silica-supported nickel catalysts [64]. The particle size distribution functions were found to be more affected by the sintering temperature than the sintering time. As sintering progressed, the distribution function developed long tails to the larger diameter side. By fitting their data to the sintering power law, the authors proposed sintering mechanisms.

Another example of the characterization of supported catalysts is the *in situ* X-ray study of Co/SiO$_2$ by Srinivasan et al. [65]. Particle sizes were calculated using both the Scherrer equation and Fourier single profile analysis. The particle size distributions are mostly bimodal, whatever the method of preparation, and 17% of the hexagonal close-packed planes were found to be faulted, i.e. every sixth plane is faulted. Insofar as surface atoms adjacent to stacking faults are sources of active sites for CO methanation and the Fischer–Tropsch synthesis, the density of active sites could be estimated.

It is important to note that it is not the particle size, but the crystallite size, which is obtained by LBA. Thus, Martin et al. [66] have shown that nickel particles were generally formed by several crystallites, unless they were prepared at very high temperatures. The fact that the crystallite size measured by LBA was much smaller than the particle size measured by SAXS and microscopy (Table 4) indicated that a fraction of the nickel particles was polycrystalline. More recently, a polydomain internal structure in nanoparticles was evidenced by Canton et al. [26] in Pd/SiO$_2$ catalysts prepared by an impregnation technique: the Fourier method gave a 2.9 nm average crystallite size whereas high-resolution microscopy gave a 5.6 nm average particle size.

3.1.2.3.5 **Whole-Powder Pattern Fitting Methods: the Rietveld Refinement** The applicability of the Scherrer equation and the classical Warren–Averbach method to

Tab. 4 Comparison between surface-weighted mean diameter $\langle D_s \rangle$ and volume-weighted mean diameter $\langle D_V \rangle$ measured by LBA, SAXS and microscopy [66]

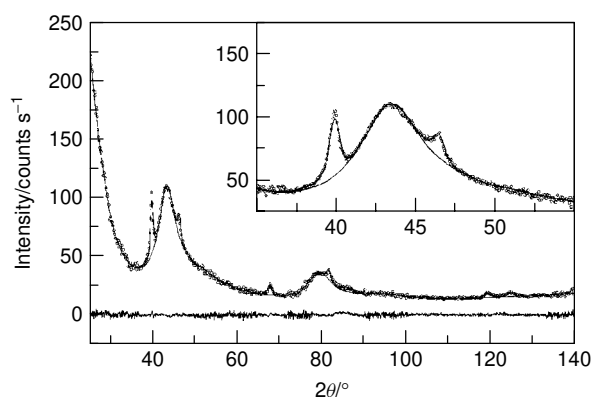| Method	$\langle D_s \rangle$/nm	$\langle D_v \rangle$/nm
LBA	17	9.5
SAXS	24	20
TEM	25	22

Fig. 8 XRD pattern of a 0.5 wt.% Pd/C catalyst sintered at 673 K fitted using a Rietveld procedure; the weighted residuals are reported at the bottom [24, 71].

catalysts is often restricted for a number of reasons. The reflections from the different solid phases [i.e. the supported metal(s) and the support] might be superimposed, for instance, in Pt/Al$_2$O$_3$ or Pd/C catalysts. Neighboring reflections such as the (111) and (200) lines in fcc metals (Ni, Cu, Rh, Pd, Ag, Ir, Pt, Au, etc.) are overlapping when the crystallites are very small. The whole-powder pattern fitting (WPPF) methods go beyond these limits by taking into account all the information available in the entire X-ray pattern.

Among the various WPPF methods, the most used is the Rietveld refinement. Some Rietveld software adapted for size–strain determination or dedicated to the microstructural analysis of materials is available on Internet [67] (for example: GSAS [68] and FullProf [69]). The Rietveld method was described in detail by Young [70]; only the part of the method dealing with particle size measurement is given below.

The method consists of fitting the experimental diffraction with a calculated one. The structure of all the phases present in the catalyst must be known. In supported metal catalysts, the metal structure is generally well known, unlike that of the support. The diffraction from an amorphous support is represented either by a polynomial function or, by the experimental pattern of the metal-free support as in the case of Fig. 8, corresponding to a Pd/C catalyst [24, 71].

The shape of XRD peaks is well described by a Voigt function, which is a convolution of Gauss and Lorentz (Cauchy) analytical functions. In a first approximation, the former function is related to strain broadening and the latter to size broadening. For microstructure analysis, the Thompson–Cox–Hastings pseudo-Voigt function is the most widely used to separate size and strain. Definitions of these functions can be found, for example, in Ref. [70].

The full width at half-maximum (FWHM) of the Gaussian and Lorentzian components of the diffraction line profile, H_G and H_L, respectively is given by

$$H_G = \left(U \tan^2 \theta + V \tan \theta + W + \frac{Z}{\cos^2 \theta} \right)^{1/2}$$

$$H_L = X \tan \theta + \frac{Y}{\cos \theta}$$

where U, V, W, X, Y and Z are the parameters to be refined and 2θ the scattering angle; U and X are related to strain (major and minor part, respectively), Y and Z to size (major and minor part, respectively) and V and W to the instrument. The instrumental parameters V and W are obtained from the preliminary refinement of a perfect standard sample giving neither size nor strain broadening (quartz, corundum, LaB$_6$, etc.). The mean particle size is obtained from Y and Z. Linear combinations of spherical harmonics allow one to model peak broadening coming from anisotropic size effects [72].

An example concerning an unsupported Ru catalyst, where the conventional LBA analysis was not applicable, is shown in Fig. 9 [73]. The three main first lines overlap and the peak shape (broad base and sharp apex) suggests a mixture of small and large particles. Indeed, the whole pattern fitting using FullProf program [69] gives mean particle sizes of 2 and 14 nm in the ratio 60 : 40.

3.1.2.3.6 Limits of Application of Methods A severe limitation comes from the lack of contrast between the intensity of the reflection and that of the overall scattering, particularly for metals with a low atomic number such as Fe, Co and Ni. Several factors – the weight fraction of metal, the difference between the square of the atomic numbers of the metal and the support and the size of the crystallites – are involved and it is not possible to state a definite limit of application of the method. Furthermore, as the amount of the phase under study decreases, the wings of the line profile become too weak to be measured and the smaller particles are not taken into account. Hence, before the method ceases to be applicable, there is a range of concentrations where LBA is increasingly less accurate. The extreme limit of size that can be measured
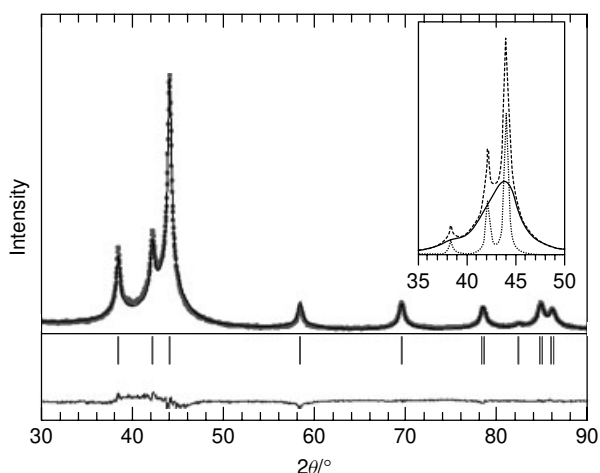
Fig. 9 Rietveld refinement of an unsupported Ru catalyst. Calculated (upper trace) and observed (dots) profiles, Ru Bragg positions and difference profile (lower trace). In the inset, calculated profiles for Ru particles: 14 nm size (dotted line); 2 nm size (solid line); mixture of 14 nm (40%) and 2 nm (60%) size (dashed line) [73].

using the classical LBA was 1.5–2 nm, but the WPPF methods should probably allow one to measure smaller sizes. There is also an upper limit of size beyond which crystallite sizes can no longer be measured because the broadening due to crystallite size becomes too small with respect to the instrumental broadening. The limit depends on the particular experimental setup and upon the error tolerated. As a rule, crystallites larger than 100 nm should not be measured by LBA.

Another important point to remember is that LBA is a bulk analysis which is sensitive to all crystallites present in the sample, irrespective of their position either on the surface of the carrier or embedded in it and therefore not accessible to the gas phase. In the case of alloys, inhomogeneities in the composition of individual particles can be the cause of the broadening of the reflection line.

3.1.2.3.7 Conclusion The Scherrer equation applied to properly corrected integral widths can give a good estimate of the mean crystallite sizes in the direction perpendicular to the reflecting planes when the particles have similar habit and a narrow size distribution. It is well suited to compare the relative size of crystallites in a series of samples (e.g. study of sintering). In the case of narrow size distributions, information on particle shape can be obtained by measuring the size perpendicular to the different reflecting planes. Scherrer analysis is widely used to determine the particle size of catalysts, often in conjunction with electron microscopy and/or chemisorption [74, 75].

Fourier analysis is much more complex and difficult to apply in practice than Scherrer analysis. More data are required (in general, different order reflections) and the entire diffraction profile must be known, including the weak tails of the profile and the background. Fourier analysis, although of relative complexity, presents important advantages over the Scherrer method. In the case of broad size distributions or bimodal distributions, only the Fourier method gives good results. The correction for instrumental broadening and strain is complete. The magnitude of the strain can be estimated and the distribution of crystallite sizes which is obtained corresponds to volume–area sizes. Therefore, the mean crystallite size is directly comparable to the size obtained by gas chemisorption.

The WPPF methods will obviously be increasingly used in the future because they allow one to characterize catalysts that are impossible to study with the classical Scherrer and Warren–Averbach methods (low metal loading, very small particles, metal and support line overlap, etc.). User-friendly software is available for the WPPF methods, but their application requires some training.

3.1.2.4 Small-Angle X-Ray Scattering Analysis

3.1.2.4.1 Introduction Small-angle X-ray scattering (SAXS) consists of X-rays scattered at low reflection angles by heterogeneities randomly distributed in solids, e.g. domains where the electron density is different from the continuous medium such as pores or metal particles in supported metal catalysts. The scattered intensity does not depend on the internal structure of the domains whether they are crystalline or amorphous. The peak of scattered intensity becomes broader as particle sizes decrease. The usual range of sizes which can be measured is 1–100 nm.

The measurement of intensities scattered near the direct beam cannot be carried out with a conventional powder diffractometer. Small-angle scattering instruments consist of an optical system providing a very thin and monochromatic X-ray beam, a sample holder and a detection system. The sample is examined by transmission. Commercial equipment associated with software for data analysis is available. SAXS has been very little used, although this technique allows not only the determination of the particle size distribution function as LBA, but also measurement of the specific surface area of the metal and of the support.

SAXS theory and applications are described in books by Brumberger [76], Glatter and Kratky [77], Feigin and Svergun [78] and Brumberger [79]. The application of SAXS to the characterization of catalysts has been reviewed by Gallezot [45], Matyi et al. [46], Renouprez [80] and Benedetti [81]. SAXS parameters are derived from an

analysis of the profile of the SAXS curve, which is a plot of the scattered intensity $I(s)$ as a function of the scattering vector q:

$$q = \left(\frac{4\pi}{\lambda}\right)\sin\theta$$

where 2θ is the scattering angle and λ the wavelength.

3.1.2.4.2 Specific Surface Area Measurements: Porod's Law

Porod [82] has shown that the surface area S between two phases of constant electron density ρ_1^e and ρ_2^e is proportional to the asymptotic value of the $q^4 I(q)$ product at large q values:

$$S = \frac{q^4 I(q)}{2\pi(\rho_1^e - \rho_2^e)^2}$$

In the case of a solid–air system, S is the specific surface area of the solid phase. The determination of the absolute value of S, expressed in $m^2\ g^{-1}$, requires the knowledge of the ratio of the scattered intensity to the incident intensity, but analogous samples may be easily compared on a relative basis. Porod's law applies whatever the shape, size distribution and concentration of the heterogeneities.

The integral scattered intensity is

$$\int_0^\infty \frac{q^2}{q^2 I(q)\,\mathrm{d}q} = 2\pi^2 V(\rho_1^e - \rho_2^e)$$

where V is the total volume of the scattering domains (i.e. pores or metal particles). Assuming a spherical form, the combination of the two previous equations gives the Porod radius R_P without going into absolute intensity measurements:

$$R_P = \left(\frac{3}{\pi}\right)\int_0^\infty \frac{q^2/I(q)\,\mathrm{d}q}{[\lim_{q\to\infty} q^4/I(q)]}$$

where R_P corresponds to a volume–area mean radius $\Sigma n_i r_i^3 / \Sigma n_i r_i^2$.

3.1.2.4.3 Mean Size Parameters: Guinier Radius

In the case of a dilute system where the scattering domains are randomly oriented and have identical shape, the SAXS curve, according to Guinier [83], can be represented in its central part by an exponential approximation:

$$I(q) = (\rho_1^e - \rho_2^e)^2 V^2 \exp\left(\frac{-q^2 R_G^2}{3}\right)$$

where R_G is the radius of gyration (or Guinier radius) of the domain. Therefore, a plot of the logarithm of the small-angle intensity versus the square of the scattering angle yields a straight line with slope proportional to R_G^2. The radius of gyration of a particle is the radius of a hypothetical sphere around the center of symmetry that both contains the total electron density of the particle and is an equivalent in X-ray scattering power to the original particle [46]. There are definite relations between R_G and the dimensions of regular solids. Thus, for a sphere of conventional radius R, $R_G^2 = (3/5)R^2$. When the particles are polydispersed, R_G is an average radius where the large particles are weighted much more heavily than the small ones.

3.1.2.4.4 Calculation of Size Distribution

When the scattering domains (i.e. pores or metal particles) are assumed to be all of equal shape but differ in size, the scattered intensity can be written as

$$I(q) = \int_0^\infty P(D)i(D,q)\,\mathrm{d}D$$

where $i(D,q)$ is the intensity scattered by a domain of diameter D and $P(D)$ is the size distribution function which represents the probability that a domain of the sample has a size between D and $D + \mathrm{d}D$. There are three types of methods to evaluate $P(D)$:

(i) The first approach supposes that the distribution has a given form. The analytical expression of the distribution function contains adjustable parameters which are fitted to match the calculated and experimental scattering curve. For instance, Whyte et al. [84] assumed a log-normal particle size distribution for Pt on alumina catalysts.

(ii) In the second approach, the distribution function is extracted directly from the scattering curve $I(s)$ by numerical analysis methods without any assumptions on the form of the distribution [85–87].

(iii) The most frequently used methods are based on the Fourier transform of the scattered intensities, which gives the correlation function $\gamma(r)$ [88] or the Patterson function $P(r)$, where $\gamma(r)$ is the size parameter in real space (see, for instance, Ref. [89]). These functions are characteristic of the geometry of the scattering domains (voids or particles). The function $\gamma(r)$ has been used to calculate chord length distributions in porous solids [90] (a chord is a segment in the scattering heterogeneity with both ends at the boundary with the continuous scattering medium). $\gamma(r)$ and $P(r)$ have also been used to calculate size distributions assuming a given particle shape.

With regard to metal-supported catalysts, volume- and surface-weighted distributions of particle sizes, and also mean sizes $\Sigma n_i d_i^4 / \Sigma n_i d_i^3$ and $\Sigma n_i d_i^3 / \Sigma n_i d_i^2$,

respectively, have very often, if not exclusively, been calculated for spherical particles.

3.1.2.4.5 Application of SAXS to Metal Particle Size Determination in Supported Catalysts

Catalyst supports are easily characterized by SAXS since they are composed of two phases, the solid and the air contained in the pores (void). The specific surface area obtained from Porod's law gives the total surface area of the pores. The application of SAXS to supported metal catalysts is not as direct. The various expressions for SAXS parameters given so far are valid for a two-phase system and supported metal catalysts constitute a three-phase system: the metal particles, the solid support and the internal void space of the support (pores).

Two approaches have been used to solve the problem, one experimental and the other based on mathematical models. The first method to be employed successfully consists of eliminating (or reducing) the magnitude of the void scattering from the support by the pore masking technique, namely the filling of the pores with a liquid of electron density similar to that of the solid support. The pore masking liquids for low-density supports are usually alkyl iodides such as CH_2I_2 [84, 91–93]. Care should be taken to avoid an excess of liquid, which would increase the overall scattering.

The second group of methods has been developed to avoid the tedious procedure of pore masking. Goodisman et al. [94], using a different analysis of the scattering curves based on a model system consisting of a grid of square cells, each cell containing either the solid support (phase 1) or the void (pores of the support, phase 2) or the metal (phase 3), were able to obtain numerical values for the specific surface area between metal and support S_{31} and metal and vacuum S_{32}. These parameters were derived from only two separate SAXS experiments on the supported catalyst and the metal-free support. Their method has been applied to Pt/Al_2O_3 catalysts [94, 95]. Shortly after, Brumberger and Goodisman [96] used the new concept of Voronoi cells to evaluate all three S_{ij} from a single experiment on the supported catalyst. Experimental application has been performed on Pt/Al_2O_3 catalysts [96] and Pt/TiO_2 [97]. Espinat et al. [98] extended the model formulated by Goodisman et al. [94] to the determination of the particle size distribution. Fairly good agreement with electron microscopy data was obtained for 1.45 and 4.5% Pt/Al_2O_3 catalysts.

In a study of 0.3–0.6 wt.% Pt/Al_2O_3, Whyte et al. [84], using the pore masking technique, showed that the Guinier radius, compared with the Porod radius or with the diameter determined from chemisorption, did not give a reliable mean size in the case of real heterodispersed catalysts, because the larger particles are weighted too heavily.

Tab. 5 Comparison between SAXS and chemisorption measurements of metal area for Pt/Al_2O_3 catalysts [91]

Pt/wt.%	$S/m^2 \ g^{-1}$		
	SAXS	H_2 chemisorption	CO chemisorption
0.6	225	243	218
2.0	125	171	156
3.7	105	105	98
4.8	90	92	87

Assuming that the metal support interface is negligibly small and that the support texture is not modified when the metal is deposited, Renouprez et al. [91] obtained the metal area by subtracting the area of the metal-free support from the total area of the catalyst. Table 5 shows that there is good agreement between the metal area determined by SAXS and by H_2 or CO chemisorption for Pt/Al_2O_3 catalysts even when the metal concentration is as low as 0.6 wt.%. The metal particle diameter distribution function was obtained with pore masking. Figure 10 shows the curve for the lowest metal concentration [80, 91], which is in good agreement with the distribution obtained by electron microscopy. It should be noted that the 5-nm particles visible on the curve correspond to a very small number of particles since the volume-weighted distribution emphasizes the large diameter values.

The distribution of the diameters of platinum particles supported on faujasite-type zeolite was obtained without pore masking [99], because zeolite pores form an ordered lattice giving low scattering and there is a high density contrast between the silicoaluminate framework and platinum. When the zeolite was activated in oxygen and reduced at 573 K, the maximum of the diameter distribution (1.1 nm) was in good agreement with the Porod diameter (1.2 nm) because all the particles were located in the zeolite supercages within a narrow size range. This situation was confirmed by hydrogen chemisorption, which indicated a dispersion of 100%. When the zeolite was activated in oxygen up to 873 K and reduced at 573 K, the diameter distribution showed that the particle size was also in the nanometer range, but the Porod area was reduced by half compared with the previous case and the amount of chemisorbed hydrogen was four times lower. Therefore, part of the metal is not taken into account by the distribution curve and the Porod area. The crystal structure analysis of the sample revealed that a large fraction of platinum was dispersed in the sodalite cages in the form of isolated atoms unable to dissociate hydrogen. This example shows that very small heterogeneities might not be taken into account by SAXS because their scattering is spread over large angles and is masked by

the background. In fact, the previous SAXS experiment was repeated using a new experimental setup to increase the sensitivity at "large" small angles. The Guinier plot, at large angles, leads to a radius of gyration of 0.25 nm, corresponding to aggregates composed of three atoms [80].

SAXS measurements on Pt/NaY catalysts were revisited by Brumberger et al. [100]. The total intensity scattered by the catalyst was approximated as a sum of contributions of the metal and the support. Metal particles were assumed to be spherical and their dispersity was represented by a Maxwell distribution. Average platinum particle diameters for different Pt/NaY catalysts and calcination temperatures are reported in Table 6.

The particle size distribution of rhodium supported on pumice, an amorphous foam constituted mostly of silica and alumina, has been investigated by Balerna et al. [101]. The radius distribution obtained by fitting the experimental SAXS pattern with a scattering curve calculated assuming a log-normal distribution of spherical metal particles is given in Fig. 11. The particle size distribution obtained by transmission electron microscopy gave larger mean diameters (27 ± 3 and 17 ± 3 Å for samples A and B, respectively). The severe discrepancy between SAXS and TEM results for sample A was explained by the presence of aggregated particles which are not resolved by TEM, which gives an apparent diameter larger than that obtained by SAXS.

3.1.2.4.6 Anomalous Small-Angle X-Ray Scattering (ASAXS)

Laboratory X-ray sources – sealed tube and rotating anode – are still used for conventional SAXS studies [24, 102, 103], but the use of synchrotron radiation is now expanding for anomalous SAXS studies. Anomalous small-angle X-ray scattering (ASAXS) is a new approach to solve the problem of the three-phase system constituted by supported metal catalysts. Indeed, the scattering by the support can be subtracted by exploiting the variation of the atomic scattering amplitude of the metal in the
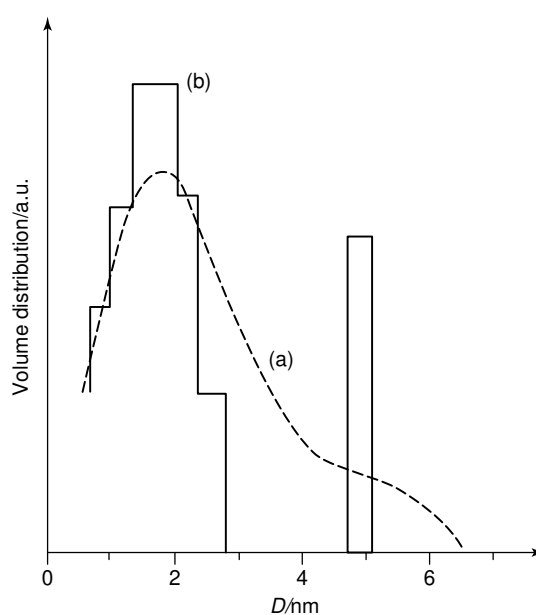

Fig. 10 Volume-weighted distribution function of metal particle sizes for a 0.6% Pt/Al$_2$O$_3$ catalyst obtained by (a) SAXS using the pore masking technique and (b) electron microscopy. (adapted from Ref. [80].).
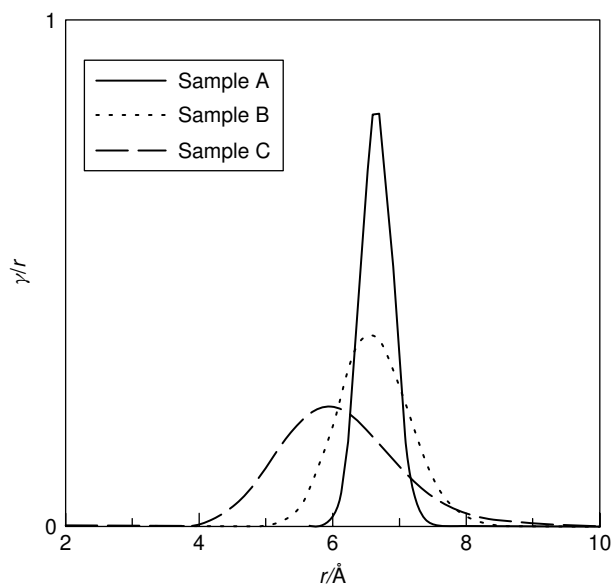

Fig. 11 Rh particle size (radius) distribution of Rh/pumice catalysts labeled as A, B, C at the respective metal loadings of 0.80, 0.46 and 0.43 wt.% [101].

neighborhood of its absorption edge. Thus, the difference between two measurements with a photon energy very near the metal adsorption edge and away gives the scattering without the support contribution.
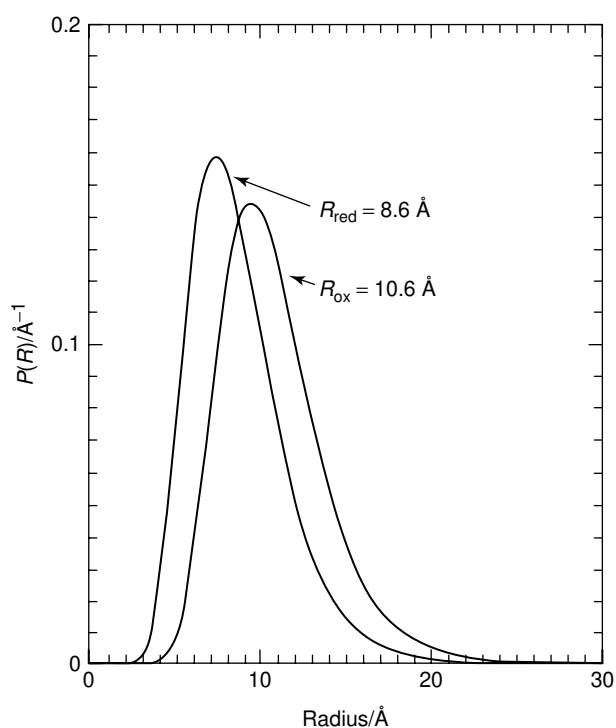
Tab. 6 Average platinum particle diameter for different Pt/NaY catalysts vs. calcination temperature after reduction at 673 K [100]

Pt/wt.%	Calcination temperature/K	Average diameter/nm
2.03	573	1.1
	673	1.6
	773	4.3
3.19	573	0.9
	673	2.1
	773	4.8
3.72	573	1.4
	673	2.2
	773	5.2

16

Fig. 12 Particle size distributions of the Pt catalyst particles in the reduced and oxidized state obtained from the fit of log-normal size distribution to the difference scattering [105].

The first ASAXS studies applied to particle size determination on catalysts were performed by Haubold and co-workers [104–106] on platinum electrocatalysts supported on porous carbon Pt/C catalysts. *In situ* measurements were made in an electrochemical cell to study both the oxidized and reduced state of platinum. The size distribution of platinum particles in a 10 wt.% Pt/C catalyst is given in Fig. 12 [105]. The anodic oxidation shifts the size distribution to larger sizes from 1.7 to 2.1 nm. It was assumed that the increase is due to the formation of an oxide surface layer.

Benedetti et al. [107] demonstrated the ability of ASAXS measurements to measure particle size in a gold catalyst supported on active carbon with a very low metal loading (0.2 wt.%). They obtained two distributions with average diameters of 1.7 and 14 nm, respectively, the former corresponding to almost 90% of the weight fraction of gold. The authors pointed out that the largest part of the metal particles, i.e. the smaller ones, remains undetected when using line broadening analysis. Two populations of different-size metal particles −1 and 14 nm – were also found on 0.72 wt.% Pd/C [108].

Brumberger et al. [109] recently demonstrated that the difference in SAXS measured at two X-ray wavelengths is equivalent to the scattering of a two-phase system. They applied this analysis to *in situ* measurements of Pt particle

size on mordenite under different atmospheres (He, O_2 and H_2) and temperatures (up to 673 K) [110].

The ASAXS technique cannot be used as a routine method because it requires a synchrotron source and gives more or less reliable results depending on the element investigated. For example, it is much less sensitive for palladium than gold [24]. Polizzi et al. [111] showed that a gold content as low as 0.2 wt.% and a Pd content of 3 wt.% could be investigated with success if optimized experimental conditions and measuring strategy were used. Moreover, until now, only four metals – Pt, Au, Pd and Ni – have been investigated (see Ref. [110] for a brief survey of the literature).

3.1.2.4.7 **Conclusion** SAXS is not very frequently used for the study of catalyst texture, probably because this technique requires special instrumentation and derivation of the size parameter is viewed as cumbersome. However, the advantages of the SAXS are often forgotten:

(i) It is a sensitive technique. Particle size distributions can be obtained for supported catalysts containing 0.5 wt.% of platinum. Furthermore, particles or clusters as small as 0.5 nm can be measured.
(ii) A complete description of the catalyst texture, including particle size, pore size and specific area, is obtained from SAXS and can be used to calculate intrinsic catalytic activity, to interpret an activity pattern as a function of particle size or to account for a particular mass transfer problem in the catalyst pores.
(iii) The size of particles constituted by several crystallites, and also the particle sizes of poorly crystalline or even amorphous solids, can still be measured by SAXS.
(iv) In contrast with electron microscopy, SAXS can be carried out *in situ* during catalyst treatments or catalytic reactions.

3.1.2.5 **Determination of Particle Size by Electron Microscopy**

3.1.2.5.1 **Scope** Electron microscopy offers the unique advantage of allowing the direct observation of catalyst morphology with a magnification tunable in the range 10^{-4}–10^{-10} m, i.e. over the entire range of particle sizes present in catalysts. Accurate data on the shape, size and spatial arrangement of particles of supports and active phases are obtained from electron microscopy images. Structural information such as symmetry and unit cell parameters of crystallites, crystal orientations (e.g. epitaxial relations between support and active phase) and lattice defects can also be obtained by electron diffraction and lattice imaging techniques. However, these structural

characterizations are not within the scope of this chapter, where the emphasis is on particle size measurements.

Three types of electron microscopes will be considered: the transmission electron microscope (TEM), which is the most commonly used tool for catalyst particle size measurement, the scanning transmission electron microscope (STEM) and the scanning electron microscope (SEM). Imaging of heterogeneous catalysts and materials containing fine particles has been described in several review articles [112–116] and in Chapter 3.1.3.3 here by Datye et al.

3.1.2.5.2 Fundamentals of Imaging and Contrast

A Transmission Electron Microscope The detailed theory of image formation, resolution and contrast in the TEM can be found in general treatises on electron microscopy and in review articles [112–116]. The point-to-point resolution in TEM is not limited by the wavelength of electrons (0.0251 Å at 200 kV), but by spherical aberrations of lenses, stability of voltage and mechanical vibrations. However, in the case of catalytic materials, the detection of small particles is mainly limited by contrast effects due to the presence of two or more solid phases (see also Chapter 3.1.3.3).

Image contrast is obtained by introducing in the back-focal plane a small objective aperture centered on the direct beam, which eliminates the scattered electrons. The image of a particle will appear darker than the background (bright-field image). Thus, particles containing elements of high atomic number will be more easily detected than particles consisting of lighter elements. Small clusters containing a few atoms will be difficult to detect, particularly if their scattering is smeared out by strong scattering from a thick and/or heavy element-containing support.

Another type of contrast is obtained by centering the objective aperture on a diffracted beam, thus excluding the unscattered beam. Then, the image of the particle is bright against a dark background; this is a so-called dark-field image where only those particles oriented to give the selected diffracted beam will be imaged. The contrast of dark-field images is usually better than that of bright-field images unless the catalyst support also gives a strong scattering at the same angle. As in the case of bright-field images, the contrast will depend on the intensity scattered by the particle and the most contrasted images will be obtained on thin supports with light atoms. An interpretation of image contrast of supported metal catalysts via image simulation methods was given by Bernal and co-workers [117, 118].

Images of lattice planes are obtained by combining one or several diffracted beams with the direct beam by letting them pass through the objective aperture. Thus, if both the (111) reflection from a cfc crystallite and the unscattered

(or 000) beam are selected by the objective aperture, they will combine and give interference fringes which are the images of stacked (111) planes. The resolution limit attained in lattice imaging is close to 1 Å.

A major limitation of TEM is that the image is a projection of the structure on the plane perpendicular to the electron beam, i.e. a particle will always appear in two dimensions. However, a 3D reconstruction can be obtained by electron tomography or 3D-TEM, a technique developed by de Jong's group [119–121]. This approach consists of recording 2D images at small angular increments while tilting the specimen over a wide angular range. The 3D reconstruction is achieved first by aligning the 2D data series then by computing via Fourier transformation the 3D image of the original object.

With the advent of high-voltage microscopes, it became possible to achieve high resolution in the presence of a low pressure of gas, thus allowing the study of changes in particle size and morphology with the nature of the atmosphere [122].

B Scanning Transmission Electron Microscope In the STEM, the electron beam is focused by lenses placed before the specimen to obtain a very small electron probe directed on to the specimen. The interaction between the electron probe and the atoms in the small irradiated volume of the specimen gives rise to different types of signals, which are recorded by specific detectors and which can be used for imaging or for analytical purposes. As the electron probe is scanned over the specimen, the intensity of one of these signals is detected, amplified and visualized on the screen of a cathode-ray tube (CRT) which is scanned synchronously with the scanning coils in the microscope column. Therefore, each "point" on the screen corresponds to a "point" (volume irradiated by the probe) on the sample and images are obtained sequentially by continuous scanning, e.g. at TV rate. The magnification is given by the ratio of the length of the video display to the length scanned on the sample and it is adjusted by changing the latter. The resolution on very thin specimens is merely given by the cross-section of the electron probe, but the resolution decreases rapidly with sample thickness because of the spreading of emitted signals in solids.

The images are formed either with the unscattered, transmitted electrons or the scattered electrons, resulting in bright- and dark-field images, respectively. The point-to-point resolution depends mainly on the size of the electron probe. The point-to-point resolution of bright-field images is not as good as in TEM, but STEMs are equipped with annular detectors that allow the efficient collection of electrons scattered at high angles, thus

allowing high-angle annular dark field (HAADF) imaging. Rutherford scattering, i.e. electrons scattered by atom nuclei at high angles, follows a Z^2 dependence. Therefore, with a very small focused electron probe (down to 3 Å) available in field emission gun (FEG) STEM, very small clusters or even single metal atoms of high nuclear charge Z can be detected (Z-contrast) [123].

Weyland et al. [124] showed that from a series of HAADF 2D images taken at various specimen tilt angles, it is possible to compute an electron tomography or 3D reconstruction of the object, thus allowing metal particles to be located on supports.

STEMs are also widely used for their analytical capabilities either with electron energy-loss spectrometry (EELS) [125] or energy-dispersive X-ray emission spectroscopy (EDX or EDS).

A new development in environmental STEM for imaging nano-objects in the liquid phase was described by Bogner et al. [126]. This so-called wet STEM was designed to record objects submerged in a liquid under annular dark-field imaging conditions.

C Scanning Electron Microscope In the SEM, the image of the specimen is formed by recording either secondary electrons or backscattered electrons emitted from the area irradiated by the scanning electron probe. The contrast is mainly due to the difference in the electron collection efficiency depending on the angle of emission and surface relief but it also depends on the atomic number of elements. The surface of the specimen should be electron conducting, which in most cases requires that the specimen surface be covered with a conducting metal layer obtained by sputtering. However, metals on electron conducting supports such as carbon can be obtained without metallic coating. Thus, a good resolution is obtained on nano-objects such as Pt particles on carbon [127] or 1 nm diameter carbon nanotubes [128].

SEM gives a high depth of field and contrasted images of specimen surfaces with a three-dimensional aspect. It is an affordable instrument which can be used by anyone after a short training period but its main drawback is the comparatively low resolution (5–10 nm), even with a small electron probe, because of beam spreading in the specimen. Particles larger than 10 nm can be detected provided that they are well isolated, but the SEM is mainly used to characterize particle sizes in the range 10^{-7}–10^{-4} m, e.g. particles of oxide, sulfide, zeolite, carbon and unsupported metals.

3.1.2.5.3 **Preparation of Samples for TEM and STEM Examination** Specimen preparation is a critical step in electron microscopy because the image quality is highly dependent on how the different solid phases are dispersed on the microscope grid and on their thickness: the thinner

the samples, the better are the resolution and contrast. Another important factor is the stability of the preparation. Thus, to retain a 0.3 nm resolution, the specimen drift should be negligible with respect to 0.3 nm during the time needed to record the micrograph. Specimens have to be deposited on 2 or 3 mm diameter copper grids (100–400 mesh), covered with a thin amorphous carbon film. Grids are available commercially or can be prepared by sputtering carbon on a collodion-covered grid and then dissolving the collodion with isoamyl acetate. For studies requiring high resolution and high contrast, the use of grids covered with holey carbon films is highly recommended. These films, punctured by many holes (usually in the range 0.2–10 µm), are available commercially. TEM observations are carried out with the solid particles across the holes.

According to the nature and thickness of the specimen, several preparation techniques are used to obtain the specimen in a form suitable for TEM observation. If the catalyst is in the form of pellets or extrudates, it should be ground into a powder. Catalyst powders with grains smaller than 50–100 nm are suitable for direct observation by TEM. The powder should be dispersed on the carbon-coated grid. The easiest way is to disperse a few milligrams of the powder ultrasonically in a few grams of water or ethanol, take a drop of the suspension, deposit it on a carbon-coated grid and let the liquid evaporate. If it is not possible to disperse the catalyst powder in a liquid (e.g. because the composition would be modified), dry deposition can be achieved by producing an aerosol of the powder and letting the aerosol settle on a grid. Unfortunately, the adherence of dry deposited particles is usually poor and this may lead to specimen instability during TEM observation.

Whenever particles are too thick for direct observation, either extractive replica or thin sections have to be made. To make extractive replicas, the catalyst powder dispersed on a sheet of mica is covered by a sputtered carbon film. The mica is then plunged into a solution of dilute hydrofluoric acid to dissolve the catalyst support without dissolving the metal particles. The carbon film with the attached metal particles is then collected on a copper grid. Extracted replicas cannot be used if the metal dispersion is modified, as in the case of first-row transition metals, which are dissolved at the same time as the support. The technique allows imaging of particles on the surface of supports too thick or containing heavy elements such as rare earth oxides. Note that only particles on the external surface of supports are extracted, which means that particles in microporous or mesoporous supports such as zeolites or carbons are not detected by this technique.

When the catalyst grains are too thick for direct observation, they can be cut into thinner sections by ultramicrotomy. The powder is embedded in a polymer

(e.g. Taab 812 resin kit) and cut into sections as thin as 20 nm with a ultramicrotome. A diamond knife is required to cut most of the solids, except α-alumina, which is too hard. This technique permits imaging of the internal morphology and metal dispersion in micro- or mesoporous catalysts (zeolites, active charcoal).

3.1.2.5.4 **Particle Size Measurement** Particle size measurements are carried out from micrographs either by image processing software from digital images or measured manually on micrographs or micrograph projections. Particle size measurements should ideally be performed on a large number of particles on several micrographs taken on different zones of a specimen grid and on several grids corresponding to different samplings of the catalyst batch. Particle size distribution can be established by measuring about 1000 particles; however, the confidence in the statistics depends greatly on particle size homogeneity. To avoid any subjective choice, particles should be measured by an independent operator. If the sizes are too dispersed, a prohibitive number of measurements would have to be performed to obtain a representative distribution. In contrast, some catalysts exhibit very narrow size distributions and therefore measurement of a few tens of particles is sufficient, provided that the size homogeneity has been checked on different sample areas. Fortunately, from a rough examination of micrographs, catalysts often fall into two classes: those with a homogeneous morphology, due to good preparation control, which can be characterized within a reasonable time (e.g. one working day), and heterogeneously dispersed catalysts, where a sound evaluation of the size distribution would require measurement of a huge number of particles; these catalysts usually do not deserve such an effort because relationships between morphology and catalytic properties cannot be unambiguously established.

Particle size can be measured with automatic image analysis. The first step is a video recording of images, which are then digitized into numerical images. Scanners are also available to provide digital images from positive photographic prints. The second step is by far the most crucial since numerical images have to be treated by various calculation routines to identify and separate the features under investigation (the particles) from all irrelevant contrast features. Finally, other routines extract morphological information, such as particle sizes, from the identified features. Automatic image processing works correctly in a limited number of cases, e.g. when the particles are sufficiently separated from each other, when the contrast with the supporting material is good enough and when particles are deposited on supports giving a uniform contrast. Computerized particle size measurements are still not widely used although they are potentially of great interest since they could replace painstaking and time-consuming manual measurements and would avoid the subjective intervention of an operator. Further progress in image treatment is needed before one can be confident enough with the technique, but control of the significance of data by experienced people will still be required in view of the morphological complexity of most industrial catalysts.

To establish a particle size distribution, a suitable size increment Δd (e.g. 1 nm) is chosen and the particles are counted in the intervals $0 - \Delta d$, $\Delta d - 2\Delta d$, ..., $n\Delta d - (n + 1)\Delta d$. The average diameter d_i for each interval is then $\Delta d/2$, $3\Delta d/2$, etc. Several types of distribution can be calculated and plotted. A practical example was given [129] where 1000 particles were measured manually on several micrographs taken on a supported metal catalyst presenting a wide size distribution; n_i is the number of particles counted in the intervals of mean diameter d_i. The number distribution (n_i vs. d_i) and the surface distribution ($n_i d_i^2$ vs. d_i) are given in Fig. 13a and b, respectively. The number distribution shows a weak maximum between 2 and 3 nm which accounts for 30% of the total number of particles. In contrast, the surface distribution shows that these particles account for only 9% of the total surface area, whereas particles between 6 and 7 nm account for 42%. Therefore, the surface distribution gives a better account of the fraction of particles making the major contribution to the total
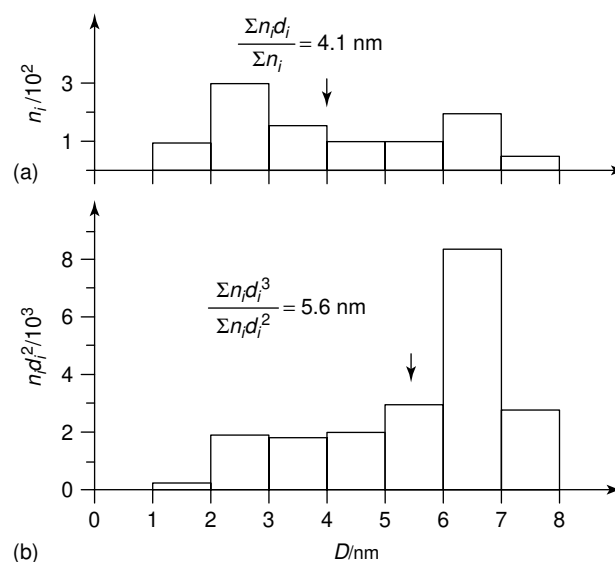

Fig. 13 (a) Number distribution and (b) face surface distribution calculated from the particle size measurements (1000 particles). Note the large difference in the profile of these distributions and in the mean size parameters (mean number diameter and mean surface diameter). (Adapted from Ref [129].)
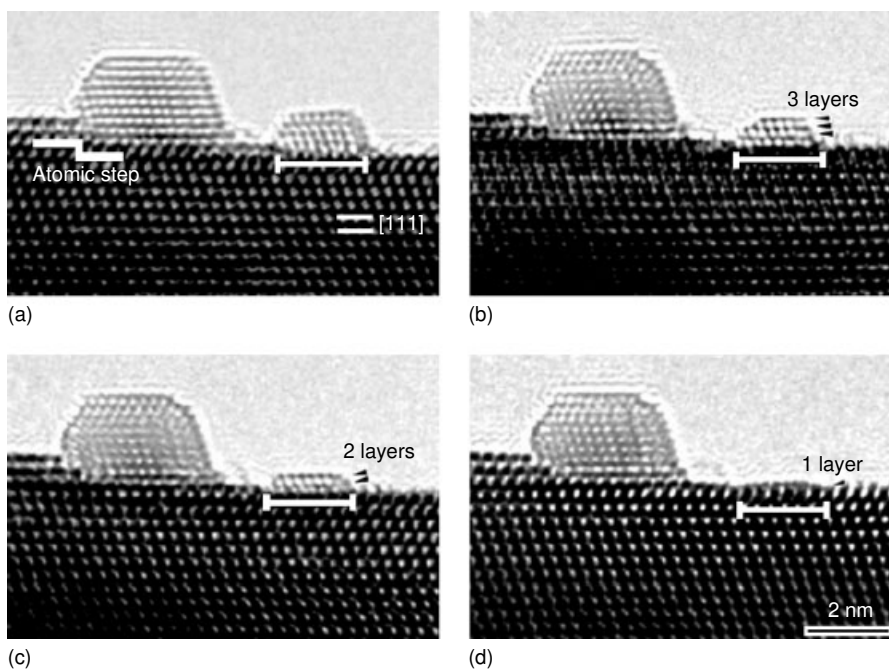
Fig. 14 Shrinking process of small Au particles on CeO$_2$ (111) facet after successive exposition to electron beam in TEM [130].

surface area and thus to the catalytic properties. In the same way, the mean surface diameter, $\Sigma n_i d_i^3 / \Sigma n_i d_i^2 = 5.6$ nm, gives more weight to the larger particles, which contribute most to the metal area, than the mean number diameter $\Sigma n_i d_i / \Sigma n_i = 4.1$ nm.

The mean surface diameter can be compared with the mean diameter calculated from surface area measurements using gas adsorption methods (Section 3.1.2.2) or with SAXS (Section 3.1.2.4). If the size distribution obtained by electron microscopy has to be compared with techniques such as X-ray line broadening and magnetic methods, sensitive to the volume of particles, the mean volume diameter $\Sigma n_i d_i^4 / \Sigma n_i d_i^3$ should be calculated.

Failure to detect particles is the main factor affecting the accuracy of particle size measurements by TEM. The usual cause is the lack of contrast of the particles with respect to the support. Thick and/or high-scattering supports will prevent the detection of small particles except those located on support edges. Particles may be undetected because of electron beam-induced changes such as shift, splitting or even vaporization of particles. These changes will depend on the energy and intensity of the electron beam and the duration of irradiation and also on particle properties such as melting point, conductivity and binding energy with supports. A striking example of particle modification on electron beam exposure is given in Fig. 14 from a TEM study of CeO$_2$-supported gold particles by Akita et al. [130], showing that the height of the thinner particle decreased as the duration of illumination increased.

Another cause of failure to detect particles is the build-up of a carbonaceous deposit on the catalyst surface by electron beam-induced decomposition of organic contaminants present in the microscope column, on the specimen grid or in the sample itself. Clean preparation of grids and specimens and a high vacuum in the column are required to avoid contamination effects preventing or reducing the visibility of particles.

Care should be taken not to overlook the presence of a few large particles which will contribute little to the total active surface but may contribute significantly to the catalyst active mass and thus lead to overestimated specific surface areas and underestimated turnover frequencies. For instance, when high-resolution TEM examination is carried out on thin sections of microporous supports, large particles on the external surface of supports, or even not associated with them, may well escape detection. In this case, direct observation of the catalyst at low magnification is highly recommended. Finally, first-row transition metals are easily oxidized in air so that their sizes are slightly larger than those of the reduced metals.

Size distributions, mean particle sizes and specific surface areas can be erroneously determined by TEM if particles have a marked two-dimensional anisotropy. Indeed, because TEM gives a projected image, it is not easy to determine the real three-dimensional morphology of particles unless they can be viewed edge-on. Tilting experiments can be useful because, unlike three-dimensional particles for which diffraction
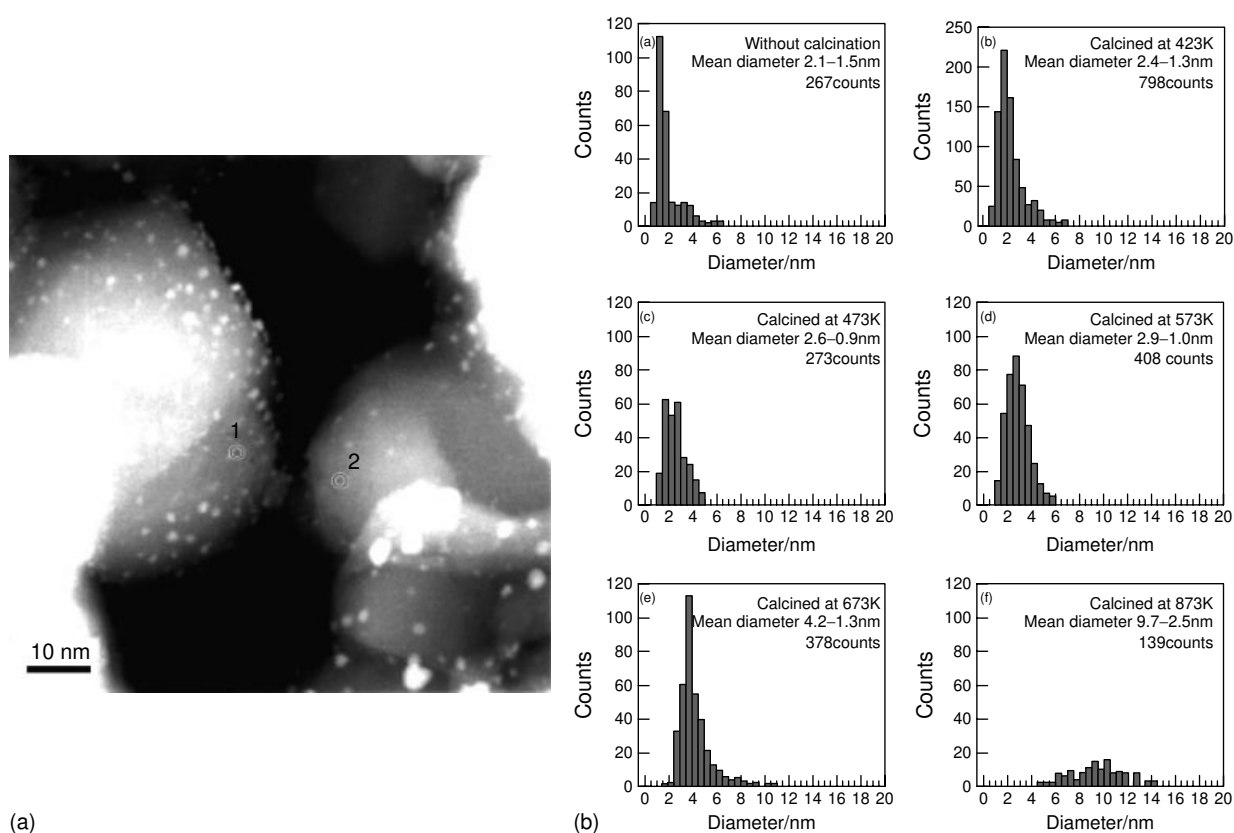
Fig. 15 (a) ADF-STEM image of Au/TiO₂ catalyst showing 2.2-nm gold particles supported on rutile and anatase phase (1 and 2, respectively). Note the difference in particle density. (b) Series of size distributions measured on TEM images of the catalyst heated at increasingly higher temperatures. Note a significant sintering at comparatively low temperatures [131].

contrast changes with tilting angle, the contrast of two-dimensional particles varies little because they give weak Bragg scattering, if any. EDX measurements can give some clues to their thickness because the X-ray emission will be lower than expected because the intensity emitted from particles of apparent diameter d will have a d^2 rather than a d^3 dependence. Better assessment of particle shape can be obtained by electron tomography (see Section 3.1.2.5.2).

3.1.2.5.5 Selected Examples of Particle Size Distribution

Because the catalytic properties of gold catalysts in oxidation and other reactions depend critically on the gold particle size, a number of studies have been devoted to determine particle size distributions. TEM observation of 1 wt.% Au/TiO₂ catalysts has been achieved to characterize the growth process of Au particles on TiO₂ upon calcining in air at different temperatures [131]. The TEM observation was performed with a JEOL JEM 3000F electron microscope operating at 300 kV. The TEM images were processed digitally and the size distributions of Au particles were performed on digital images using

the image analyzing software Image-Pro. Figure 15 is an ADF-STEM image of Au/TiO₂ catalyst before calcination. The density of Au-particles is much higher on area 1 than on area 2, which correspond to rutile and anatase phases, respectively. Figure 15 gives the particle size distribution as the catalyst was calcined up to 873 K, showing that particle sintering occurs significantly even at low temperatures.

Model gold catalysts have been prepared on γ-Al₂O₃, TiO₂ and ZrO₂ supports by laser vaporization of gold [132]. Particle size measurements on TiO₂ and ZrO₂ were carried out on extractive replicas. Figure 16a and b give the particle size distribution on the three supports obtained before and after oxidation of CO. The mean particle diameters were nearly identical on the three supports, within 10%, indicating that the vaporization produces clusters of the same size whatever the support. After reaction (Fig. 16b), the particles have a mean diameter larger than that of the fresh catalyst, but the sintering depends slightly on the nature of the support.
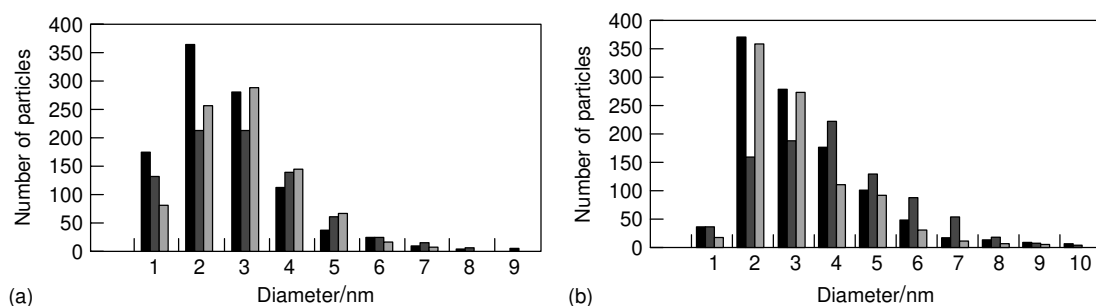
Fig. 16 (a) Size distribution of gold clusters prepared by laser vaporization on γ-Al_2O_3 (black), ZrO_2 (dark gray) and TiO_2 (light gray). (b) Size distribution of gold clusters after CO oxidation reaction [132].
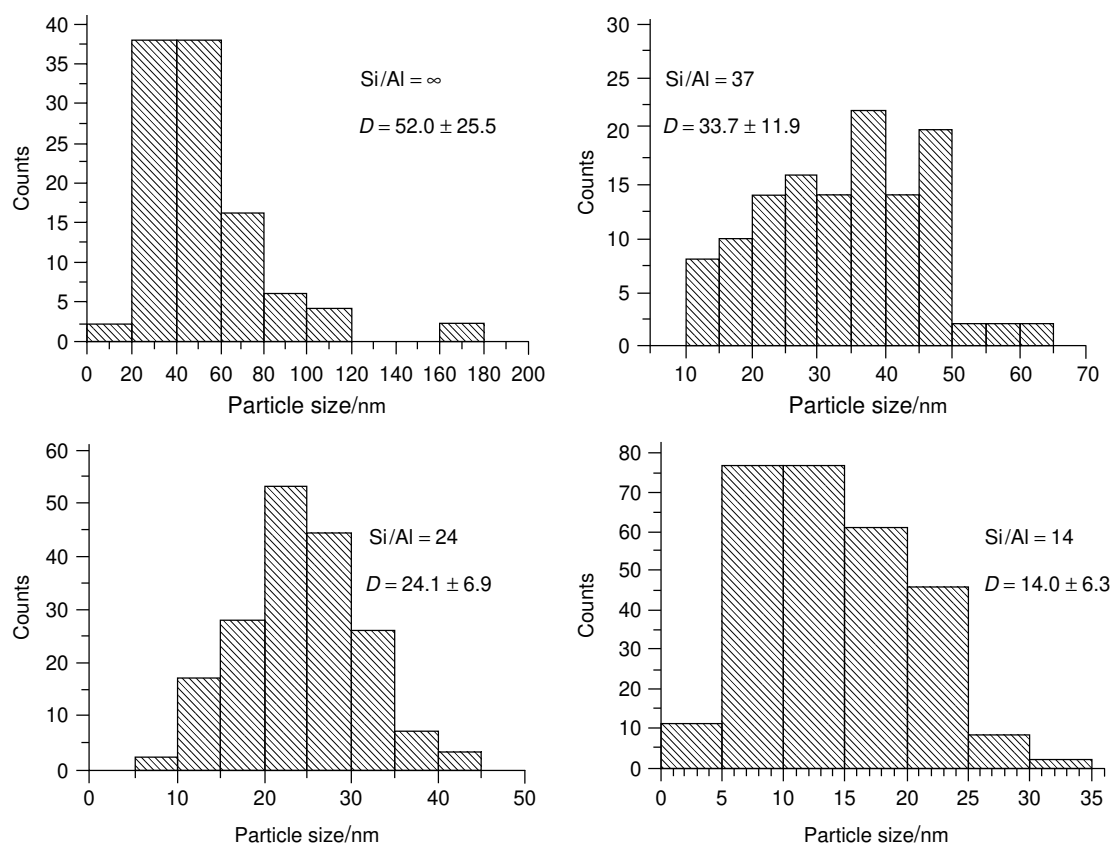

Fig. 17 Size distribution of Au−Ag particles deposited on mesoporous supports with different Si/Al ratios [135].

Gold, nickel and gold−nickel alloy deposited on carbon film by laser vaporization also give similar particle size distributions centered at 2.2 nm [133]. The control of highly reproducible syntheses of gold catalysts supported on TiO_2 by deposition−precipitation or by impregnation has been achieved by TEM [134]. It was also shown that during CO oxidation Au particles grow from less than 2 nm to 3−4 nm.

Au−Ag bimetallic particles supported on mesoporous aluminosilicates with different Si/Al ratios were studied by Wang et al. [135]. The catalytic activity in CO oxidation depended markedly on the Si : Al ratio. This was correlated with the particle size distribution (Fig. 17), showing that the particle size depends also markedly on the Si : Al ratio.

In a number of cases, metal or oxide particles cannot be detected on TEM micrographs because the contrast is low with respect to high molecular weight support. Thus, detection of Pd−Ni bimetallic particles supported on mixed oxides $Ce_{0.5}Zr_{0.5}O_2$ and $Ce_{0.5}Zr_{0.5}O_2/Al_2O_3$ was not possible with TEM because of the lack of contrast

(a) (b) (c)

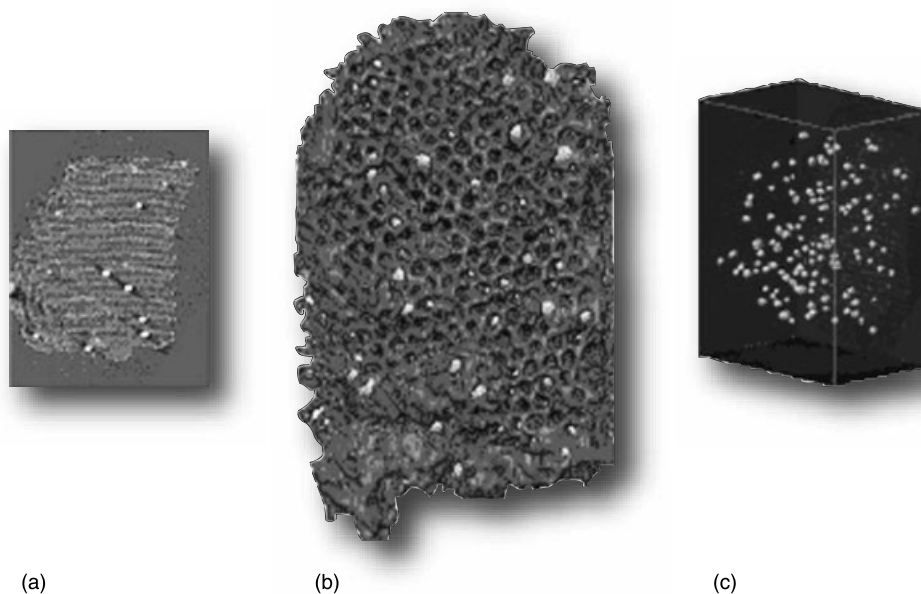**Fig. 18** (b) Reconstructed density of an Au/SBA-15 catalyst particle (256 × 256 × 166 nm) obtained by electron tomography. (a) Virtual cross-section (0.64 nm thickness through the reconstruction. (c) 3D spatial distribution of gold particles [120].

with the support [136]. The size distributions of particles were obtained from micrographs taken with a high-angle annular dark field detector (Z-contrast) in a FEG-STEM. Z-contrast imaging with FEG-STEM was also used by Sun et al. [137] to follow the formation of Pd–Cu bimetallic catalysts on γ-Al$_2$O$_3$ as a function of the reduction temperature. This study was coupled with EELS analysis to monitor alloy composition. Co$_3$O$_4$ particles in Co/TiO$_2$ Fischer–Tropsch catalysts were also detected on annular dark-field images taken in a dedicated FEG-STEM [138].

3.1.2.5.6 Selected Examples of 3D Localization of Particles in Supports by Electron Tomography
Electron tomography, described briefly in Section 3.1.2.5.2A, has been used extensively by de Jong's group to determine the position and measure the size of particles encapsulated in various supports. Thus, a 3D reconstruction of a grain of mesoporous SBA-15 containing gold particles was computed from 151 projection images taken from −55 to +55°. Figure 18 gives the 3D reconstruction of a particles of SBA-15 showing clearly the localization of gold in the pores [120].

Another striking example of electron tomography is provided by the assessment of 3D localization of Pd particles within a silica support synthesized by the sol–gel process. Electron tomography (Fig. 19) shows that the small Pd particles are localized deep inside the silica skeleton whereas large particles are outside [121]. The particles are regularly spaced with a distance between them comparable to the diameter of the struts of silica.

3.1.2.6 Particle Size Measurements by Magnetic Methods
Magnetic methods for the study of the particle size of catalysts were pioneered by Selwood [139] and reviewed by Dalmon [140]. When a ferromagnetic metal is highly divided, e.g. in the form of particles smaller than ca. 20 nm, the particles consist of single magnetic domains with a magnetic moment μ proportional to the volume of the particles:

$$\mu = \left(\frac{\pi \rho \sigma_s}{6}\right) D^3$$

where ρ is the mass density, σ_s the saturation magnetization per unit mass and D the particle diameter. In these superparamagnetic solids, the moments μ are randomly oriented except when they are placed in an external magnetic field, H. Then, they behave like an assembly of paramagnetic atoms, i.e. the external field exerts a force, μH, on them which tends to orientate them parallel to the field. In the presence of moderate fields, the largest particles, which have the largest moments, will respond first to the force μH, which will orientate them in the direction of the field. For smaller particles with lower moments, the thermal agitation will be high enough to maintain a random distribution of their magnetic moments. They will orientate at higher fields and/or at lower temperatures. The saturation magnetization, M_s, is reached when all the moments are oriented.
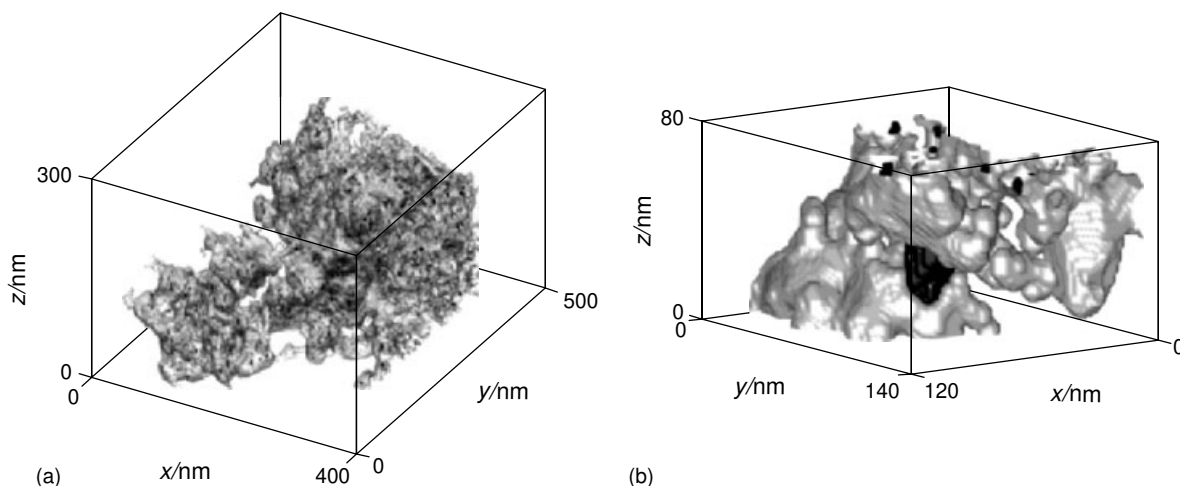
Fig. 19 (a) 3D view of 3.1 wt.% Pd/SiO$_2$. The fine Pd particles are encapsulated in the Xerogel. The sample was cut so that part of the interior of the silica is visible. (b) Another 3D reconstruction showing that large Pd particles are outside the silica skeleton [121].

The magnetization of superparamagnetic particles follows a Langevin-type function:

$$M = M_s \left[\coth\left(\frac{\mu H}{kT}\right) - \left(\frac{kT}{\mu H}\right) \right]$$

At high $H : T$ ratios, this equation simplifies to

$$M = M_s \left[1 - \left(\frac{kT}{\mu H}\right) \right]$$

so that the saturation magnetization can be obtained by extrapolation to $1/H = 0$ of the plot of M vs. $1/H$. The amount of reduced metal can be calculated from M_s. As an example, Fig. 20a gives the magnetization curve measured at 300 K of 55 mg of Ni/SiO$_2$ catalyst containing 20.8% nickel and Fig. 20b shows the extrapolation of M at low fields, giving a saturation magnetization $M_s = 0.618$ emu cgs. Since $\sigma_s(\text{Ni}) = 54.4$ emu cgs, the amount of reduced nickel is $0.618/54.4 = 11.4 \times 10^{-3}$ g and the extent of nickel reduction is $100 \times 11.4/(55 \times 0.208) = 99.7\%$ [140].

From the slopes of the magnetization curves at low and high fields, it is possible to calculate the diameters D_1 and D_2 of the larger and smaller particles, respectively. The difference between D_1 and D_2 gives an estimate of the particle size heterogeneity.

Magnetic methods are better suited to determine the particle size of iron, cobalt and nickel than X-ray methods and electron microscopy, which are less sensitive. Indeed, a metal content as small as 100 ppm can be detected and the accuracy on average size is 1%. The upper size limit is ca. 15 nm while there is, in principle, no lower limit for size determination if low-temperature cryogenic baths are available.
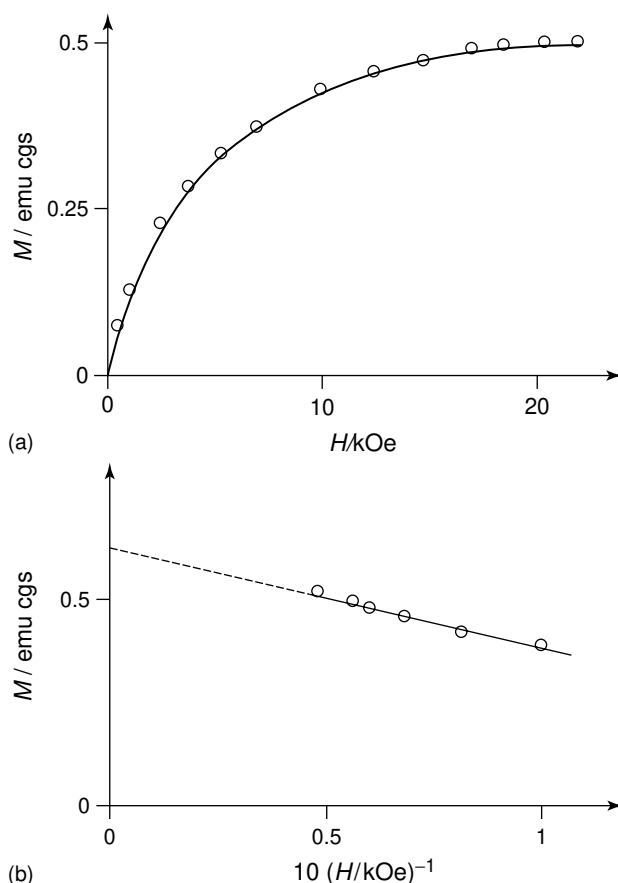

Fig. 20 (a) Magnetization curve of an Ni/SiO$_2$ sample ($T = 300$ K, $m = 55$ mg, 20.8 wt.% Ni); (b) extrapolation at $1/H = 0$ of the magnetization M. (Adapted from Ref. [140].)

The method has been applied to measure the size distribution of cobalt particles supported on SiO$_2$ [141].

25

Tab. 7 Comparison between magnetic and microscopy measurements of average particle size for Co/SiO$_2$ catalysts [141]

Co loading/wt.%	D_s/nm	
	Magnetic method	TEM
1.65	4.6	5.0
4.78	6.2	6.9
7.56	7.8	8.6

The average diameters measured by the magnetic method and TEM are in good agreement, as shown in Table 7.

Recently magnetic measurements under steam reforming of ethanol were performed on various cobalt catalysts [142]. The amount of metallic cobalt was determined as a function of temperature and hydrogen partial pressure, showing that there is an easy exchange between reduced and oxidized cobalt species.

References

1. R. van Hardeveld, F. Hartog, *Surf. Sci.* **1969**, *15*, 189.
2. (a) A. L. Mackay, *Acta Crystallogr.* **1962**, *15*, 916; (b) M. B. Gordon, *PhD Thesis*, Grenoble, 1978.
3. B. E. Sundquist, *Acta Metall.* **1964**, *12*, 67.
4. J. R. Anderson, *Structure of Metallic Catalysts*, Academic Press, London, 1975, p. 296.
5. J. F. Scholten, in *Preparation of Catalysts II, Scientific Bases for the Preparation of Heterogeneous Catalysts*, B. Delmon, P. Grange, P. Jacobs, G. Poncelet (Eds.), Elsevier, Amsterdam, 1979, p. 685.
6. J. R. Anderson, *Structure of Metallic Catalysts*, Academic Press, London, 1975, p. 295.
7. J. J. F. Scholten, A. P. Pijpers, A. M. L. Hustings, *Catal Rev. Sci. Eng.* **1985**, *27*, 151.
8. P. G. Menon, in *Hydrogen Effects in Catalysis; Fundamentals and Practical Applications*, Z. Paál, P. G. Menon (Eds.), Marcel Dekker, New York, 1987, Vol. 31, Chapter 4, p. 117.
9. C. H. Bartholomew, in *Catalysis, Specialist Periodical Reports*, Vol. 11, Royal Society of Chemistry, London, 1994, Chapter 3, p. 93.
10. *Determination of the Specific Surface Area of Powders. Recommendations for Methods of Determination of Metal Surface Area Using Gas Adsorption Techniques.* British Standard, 4359-4, 1995.
11. J. A. Anderson, M. Fernandez-Garcia, A. Martinez-Arias, in *Supported Metals in Catalysis*, J. A. Anderson, M. Fernandez-Garcia (Eds.), *Catalytic Science Series*, Vol. 5, Imperial College Press, London, 2005, Chapter 4, p. 123.
12. B. C. Lippens, B. G. Linsen, J. H. de Boer, *J. Catal.* **1964**, *3*, 32.
13. G. J. Den Otter, F. M. Dautzenberg, *J. Catal.* **1978**, *53*, 116.
14. P. B. Wells, *Appl. Catal.* **1985**, *18*, 259.
15. A. Hausen, H. L. Gruber, *J. Catal.* **1971**, *20*, 97.
16. A. Frennet, P. B. Wells, *Appl. Catal.* **1985**, *18*, 243.
17. K. Kunimori, T. Uchijima, M. Yamada, H. Matsumoto, T. Hattori, Y. Murakami, *Appl. Catal.* **1982**, *4*, 67.
18. P. G. Menon, J. Sieders, F. Streefkerk, G. J. M. van Keulen, *J. Catal.* **1973**, *29*, 188.
19. J. L. Falconner, J. A. Schwarz, *Catal. Rev. Sci. Eng.* **1983**, *25*, 141.
20. K. Foger, in *Catalysis: Science and Technology*, J. R. Anderson, M. Boudart (Eds.), Springer, Berlin, 1984, Vol. 6, Chapter 4, p. 227.
21. N. Krishnankutty, M. A. Vannice, *J. Catal.* **1995**, *155*, 312.
22. L. Bednarova, C. E. Lyman, E. Rytter, A. Holmen, *J. Catal.* **2002**, *211*, 335.
23. S. Lambert, B. Heinrichs, A. Brasseur, A. Rulmont, J.-P. Pirard, *Appl. Catal. A* **2004**, *270*, 201.
24. G. Fagherazzi, P. Canton, P. Riello, N. Pernicone, F. Pinna, M. Battagliarin, *Langmuir* **2000**, *16*, 4539.
25. P. Canton, G. Fagherazzi, M. Battagliarin, F. Menegazzo, F. Pinna, N. Pernicone, *Langmuir* **2002**, *18*, 6530.
26. P. Canton, F. Menegazzo, S. Polizzi, F. Pinna, N. Pernicone, P. Riello, G. Fagherazzi, *Catal. Lett.* **2003**, *88*, 141.
27. A. Beck, A. Horváth, A. Szücs, Z. Schay, Z. E. Horváth, Z. Zsoldos, I. Dékány, L. Guczi, *Catal. Lett.* **2000**, *65*, 33.
28. G. Bergeret, P. Gallezot, P. Gélin, Y. Ben Taarit, F. Lefebvre, C. Naccache, R. D. Shannon, *J. Catal.* **1987**, *104*, 279.
29. M. Primet, M. El Azhar, R. Fréty, M. Guénin, *Appl. Catal.* **1990**, *59*, 153.
30. E. Rogemond, N. Essayem, R. Fréty, V. Perrichon, M. Primet, M. Chevrier, C. Gauthier, F. Mathis, *Catal Today* **1996**, *29*, 83.
31. V. Perrichon, L. Retailleau, P. Bazin, M. Daturi, J. C. Lavalley, *Appl. Catal. A* **2004**, *260*, 1.
32. H. Berndt, U. Müllet, *Appl. Catal. A* **1999**, *180*, 63.
33. R. L. Moss, in *Experimental Methods in Catalytic Research*, R. B. Anderson, P. T. Dawson (Eds.), Academic Press, New York, 1976, Vol. 2, p. 43.
34. D. J. O'Rear, D. G. Löffler, M. Boudart, *J. Catal.* **1990**, *121*, 131.
35. *Standard Test Method for Hydrogen Chemisorption on Supported Platinum on Alumina Catalysts and Catalyst Carriers by Volumetric Vacuum Method*, ASTM D3908-03, ASTM International, on line www.astm.org, and in *Annual Book of ASTM Standards*, ASTM, Philadelphia, PA, Vol. 05.05.
36. Y. Murakami, in *Preparation of Catalysts III, Scientific Bases for the Preparation of Heterogeneous Catalysts*, G. Poncelet, P. Grange, P. A. Jacobs (Eds.), Elsevier, Amsterdam, 1983, p. 775.
37. J. E. Benson, M. Boudart, *J. Catal.* **1965**, *4*, 704.
38. G. Prelazzi, M. Cerboni, G. Leofanti, *J. Catal.* **1999**, *181*, 73.
39. W. C. Conner, in *Hydrogen Effects in Catalysis; Fundamentals and Practical Applications*, Z. Paál, P. G. Menon (Eds.), Marcel Dekker, New York, 1987, Vol. 31, p. 311.
40. C. R. Adams, H. A. Benesi, R. M. Curtis, R. G. Mesenheimer, *J. Catal.* **1962**, *1*, 336.
41. J. E. Benson, H. S. Hwang, M. Boudart, *J. Catal.* **1973**, *30*, 146.
42. Y. Ji, A. M. J. van der Eerden, V. Koot, P. J. Kooyman, J. D. Meeldijk, B. M. Weckhuysen, D. C. Koningsberger, *J. Catal.* **2005**, *234*, 376.
43. J. Prasad, K. R. Murthy, P. G. Menon, *J. Catal.* **1978**, *52*, 515.
44. F. Locatelli, B. Didillon, D. Uzio, G. Niccolai, J. P. Candy, J. M. Basset, *J. Catal.* **2000**, *193*, 154.
45. P. Gallezot, in *Catalysis: Science and Technology*, J. R. Anderson, M. Boudart (Eds.), Springer, Berlin, 1984, Vol. 5, p. 221.
46. R. J. Matyi, L. R. Schwartz, J. B. Butt, *Catal. Rev. Sci. Eng.* **1987**, *29*, 41.
47. J. I Langford, in *Diffraction Analysis of the Microstructure of Materials*, E. J. Mittemeijer, P. Scardi (Eds.), *Springer Series in Materials Science*, Vol. 68, Springer, Berlin, 2004, p. 3.

48. R. L. Snyder, J. Fiala, H. J. Bunge, *Defect and Microstructure Analysis by Diffraction, IUCr Monographs on Crystallography*, Vol 10, International Union of Crystallography, Oxford University Press, Oxford, 1999, 785 pp.

49. E. J. Mittemeijer, P. Scardi, *Diffraction Analysis of the Microstructure of Materials, Springer Series in Materials Science*, Vol. 68, Springer, Berlin, 2004, 549 pp.

50. P. Scherrer, *Göttingen Nachr.* **1918**, *2*, 98.

51. A. R. Stokes, A. J. C. Wilson, *Proc. Camb. Philos. Soc.* **1942**, *38*, 313.

52. J. I. Langford, A. J. C. Wilson, *J. Appl. Crystallogr.* **1978**, *11*, 102.

53. B. E. Warren, *J. Appl. Phys.* **1941**, *12*, 375.

54. B. E. Warren, B. L. Averbach, *J. Appl. Phys.* **1950**, *21*, 595.

55. B. E. Warren, *X-Ray Diffraction*, Addison-Wesley, Reading, MA, 1969, Chapter 13, p. 251.

56. A. R. Stokes, *Proc. Phys. Soc. London* **1948**, *61*, 382.

57. B. Moraweck, P. de Montgolfier, A. J. Renouprez, *J. Appl. Crystallogr.* **1977**, *10*, 184.

58. P. Ganesan, H. K. Kuo, A. Saavedra, R. J. de Angelis, *J. Catal.* **1978**, *52*, 310.

59. F. Bertaut, *Acta Crystallogr.* **1950**, *3*, 14.

60. W. L. Smith, *J. Appl. Crystallogr.* **1972**, *5*, 127.

61. B. Moraweck, P. de Montgolfier, A. J. Renouprez, *J. Appl. Crystallogr.* **1977**, *10*, 191.

62. S. R. Sashital, J. B. Cohen, R. L. Burwell Jr., J. B. Butt, *J. Catal.* **1977**, *50*, 479.

63. P. H. Otero-Schipper, W. A. Wachter, J. B. Butt, R. L. Burwell Jr., J. B. Cohen, *J. Catal.* **1977**, *50*, 494.

64. H. K. Kuo, P. Ganesan, R. J. de Angelis, *J. Catal.* **1980**, *64*, 303.

65. R. Srinivasan, R. J. de Angelis, P. J. Reucroft, A. G. Dhere, J. Bentley, *J. Catal.* **1989**, *116*, 144.

66. G. A. Martin, B. Moraweck, A. J. Renouprez, G. Dalmai, B. Imelik, *J. Chim. Phys.* **1972**, 532.

67. Collaborative Computational Project Number 14 (CCP14), http://www.ccp14.ac.uk/solution/rietveld_software.

68. A. C. Larson, R. B. Von Dreele, *General Structure Analysis System (GSAS)*, Los Alamos National Laboratory, University of California, Los Alamos, CA, Report LAUR, 2004, 86−748.

69. J. Rodríguez-Carvajal, FullProf, http://www.ill.fr/dif/soft/fp and http://www.ccp/web-mirrors/fullproof.

70. R. A. Young, *The Rietveld Method, IUCr Monographs on Crystallography*, Vol 5, International Union of Crystallography, Oxford University Press, Oxford, 1993, 298 pp.

71. G. Fagherazzi, P. Canton, P. Riello, F. Pinna, N. Pernicone, *Catal. Lett.* **2000**, *64*, 116.

72. J. Rodriguez-Carvajal, Rietveld refinement of complex inorganic materials using FullProf, presented at the 21st European Crystallographic Meeting, Crystallographic Software Workshop, Durban, 2003, http://www.ccp14.ac.uk/projects/ecm21-durban2003/juan/ecm21_fullprof_juan.pdf.

73. K. Pelzer, J.-P. Candy, G. Bergeret, B. Chaudret, J.-M. Basset, to be published.

74. G. Neri, M. G. Musolino, C. Milone, D. Pietropaolo, S. Galvagno, *Appl. Catal. A* **2001**, *208*, 307.

75. S. Yang, C. Liang, R. Prins, *J. Catal.* **2006**, *237*, 118.

76. H. Brumberger (Ed.), *Small-Angle X-Ray Scattering*, Gordon and Breach, New York, 1965.

77. O. Glatter, O. Kratky (Eds.), *Small Angle X-Ray Scattering*, Academic Press, London, 1982.

78. L. A. Feigin, D. I. Svergun, *Structure Analysis by Small-Angle X-Ray and Neutron Scattering*, Plenum Press, New York, 1987.

79. H. Brumberger (Ed.), *Modern Aspects of Small-Angle Scattering, Proceedings of the NATO Advanced Study Institute on Modern Aspects on Small-Angle Scattering, Como, May 1993, NATO ASI Series*, Kluwer, Dordrecht, 1995.

80. (a) A. J. Renouprez, in *Les Techniques Physiques d'Etude des Catalyseurs*, B. Imelik, J. C. Védrine (Eds.), Technip, Paris, 1988, p. 633; (b) A. J. Renouprez, in *Catalyst Characterization: Physical Techniques for Solid Materials*, B. Imelik, J. C. Védrine (Eds.), Plenum Press, New York, 1994, p. 445.

81. A. Benedetti, *J. Appl. Crystallogr.* **1997**, *30*, 647.

82. (a) G. Porod, *Z. Kolloid.* **1951**, *124*, 83; (b) G. Porod, *Z. Kolloid.* **1952**, *125*, 51; (c) G. Porod, *Z. Kolloid.* **1952**, *125*, 109.

83. (a) A. Guinier, *X-Ray Diffraction in Crystals, Imperfect Crystals and Amorphous Bodies*, Freeman, San Francisco, 1963, p. 319; (b) A. Guinier *Théorie et Technique de la Radiocristallographie*, 3rd Ed., Dunod, Paris, 1964, p. 637.

84. T. E. Whyte Jr., P. W. Kirklin, R. W. Gould, H. Heinemann, *J. Catal.* **1972**, *25*, 407.

85. C. G. Vonk, *J. Appl. Crystallogr.* **1976**, *9*, 433.

86. O. Glatter, *J. Appl. Crystallogr.* **1977**, *10*, 415.

87. D. I. Svergun, A. V. Semenyuk, L. A. Feigin, *Acta Crystallogr. A* **1988**, *44*, 244.

88. I. S. Fedorova, P. W. Schmidt, *J. Appl. Crystallogr.* **1978**, *11*, 405.

89. H. Brusset, J. R. Donati, *J. Appl. Crystallogr.* **1969**, *2*, 55.

90. J. Méring, D. Tchoubar, *J. Appl. Crystallogr.* **1968**, *1*, 153.

91. A. Renouprez, C. Hoang-Van, P. A. Compagnon, *J. Catal.* **1974**, *34*, 411.

92. G. Cocco, L. Schiffini, G. Strukul, *J. Catal.* **1980**, *65*, 348.

93. T. Lopez, M. Asomoza, P. Bosch, E. Garcia-Figueroa, R. Gomez, *J. Catal.* **1992**, *138*, 463.

94. J. Goodisman, H. Brumberger, R. Cupelo, *J. Appl. Crystallogr.* **1981**, *14*, 305.

95. R. K. Nandi, F. Molinaro, C. Tang, J. B. Cohen, J. B. Butt, R. L. Burwell Jr., *J. Catal.* **1982**, *78*, 289.

96. H. Brumberger, J. Goodisman, *J. Appl. Crystallogr.* **1983**, *16*, 83.

97. H. Brumberger, F. Delaglio, J. Goodisman, M. G. Phillips, J. A. Schwarz, P. Sen, *J. Catal.* **1985**, *92*, 199.

98. D. Espinat, B. Moraweck, J. F. Larue, A. J. Renouprez, *J. Appl. Crystallogr.* **1984**, *17*, 269.

99. P. Gallezot, A. Alarcon-Diaz, J. A. Dalmon, A. J. Renouprez, B. Imelik, *J. Catal.* **1975**, *39*, 334.

100. H. Brumberger, J. G. Goodisman, R. Ramaya, S. Ciccariello, *J. Appl. Crystallogr.* **1996**, *29*, 526.

101. A. Balerna, S. Coluccia, G. Deganello, A. Longo, A. Martorana, G. Martra, C. Meneghini, P. Pertici, G. Pipitone, E. Pitzalis, A. M. Venezia, A. Verrazzani, G. Vitulli, *Eur. Phys. J. D* **1999**, *7*, 577.

102. A. Barrera, M. Viniegra, P. Bosch, V. H. Lara, S. Fuentes, *Appl. Catal. B* **2001**, *34*, 97.

103. L. F. Liotta, A. Longo, A. Macaluso, A. Martorana, G. Pantaleo, A. M. Venezia, G. Deganello, *Appl. Catal. B* **2004**, *48*, 133.

104. H. G. Haubold, X. H. Wang, *Nucl. Instrum. Methods B* **1995**, *97*, 50.

105. H. G. Haubold, X. H. Wang, H. Jungbluth, G. Goerigk, W. Schilling, *J. Mol. Struct.* **1996**, *383*, 283.

106. H. G. Haubold, X. H. Wang, G. Goerigk, W. Schilling, *J. Appl. Crystallogr.* **1997**, *30*, 653.

107. A. Benedetti, S. Polizzi, P. Riello, F. Pinna, G. Goerigk, *J. Catal.* **1997**, *171*, 345.

108. A. Benedetti, L. Bertoldo, P. Canton, G. Goerigk, F. Pinna, P. Riello, S. Polizzi, *Catal. Today* **1999**, *49*, 485.

109. H. Brumberger, D. Hagrman, J. Goodisman, K. D. Finkelstein, *J. Appl. Crystallogr.* **2005**, *38*, 147.

110. H. Brumberger, D. Hagrman, J. Goodisman, K. D. Finkelstein, *J. Appl. Crysallogrt.* **2005**, *38*, 324.

111. S. Polizzi, P. Riello, G. Goerigk, A. Benedetti, *J. Synchrotron Radiat.* **2002**, *9*, 65.

112. M. Jose-Yacaman, M. Avalos-Borja, *Catal.Rev. Sci. Eng.* **1992**, *34*, 55.

113. A. K. Datye, *Catal.Rev. Sci. Eng.* **1992**, *34*, 129.

114. J. M. Thomas, O. Terasaki, *Top. Catal.* **2002**, *21*, 155.

115. A. K. Datye, *J. Catal.* **2003**, *216*, 144.

116. J. Liu, *J. Electron Microsc.* **2005**, *54*, 251.

117. S. Bernal, F. J. Botana, J. J. Calvino, G. A. Cifredo, J. A. Perez-Omil, J. M. Pintado, *Catal. Today* **1995**, *23*, 219.

118. S. Bernal, F. J. Botana, J. J. Calvino, C. Lopez-Cartes, J. A. Perez-Omil, J. M. Rodriguez-Izquierdo, *Ultramicroscopy* **1998**, *72*, 135.

119. A. J. Koster, U. Ziese, A. J. Verkleij, A. H. Hansen, K. P. de Jong, *J. Phys. Chem. B* **2000**, *104*, 9368.

120. U. Ziese, K. P. de Jong, A. J. Koster, *J. Phys. Chem. B* **2003**, *107*, 10552.

121. C. J. Gommes, K. P. de Jong, J. P. Pirard, S. Blacher, *Langmuir* **2005**, *21*, 12378.

122. P. L. Hansen, J. B. Wagner, S. Helveg, J. R. Rostrup-Nielsen, B. S. Clausen, H. Topsoe, *Science* **2002**, *295*, 2053.

123. S. J. Pennycook, B. Rafferty, P. D. Nellist, *Microsc. Microanal.* **2000**, *6*, 343.

124. M. Weyland, P. A. Midgley, J. M. Thomas, *J. Phys. Chem. B* **2001**, *105*, 7882.

125. C. Colliex, M. Tence, E. Lefevre, C. Mory, H. Gu, D. Bouchet, C. Jeanguillaume, *Mikrochim. Acta* **1994**, *114/115*, 71.

126. A. Bogner, G. Thollet, D. Basset, P. H. Jouneau, C. Gauthier, *Ultramicroscopy* **2005**, *104*, 290.

127. J. Liu, *Microsc. Microanal.* **2000**, *6*, 388.

128. E. D. Boyes, *Microsc. Microanal.* **2000**, *6*, 307.

129. P. Gallezot, C. Leclercq, in *Catalyst Characterization, Physical Techniques for Solid Materials, Fundamental and Applied Catalysis*, B. Imelik, J. C. Vedrine (Eds.), Plenum Press, New York, 1994, p. 509.

130. T. Akita, M. Okumara, K. Tanaka, M. Koyama, M. Haruta, *J. Mater. Sci.* **2005**, *40*, 3101.

131. T. Akita, P. Lu, S. Ichikawa, K. Tanaka, M. Haruta, *Surf. Interface Anal.* **2001**, *31*, 73.

132. S. Arrii, F. Morfin, A. J. Renouprez, J. L. Rousset, *J. Am. Chem. Soc.* **2004**, *126*, 1199.

133. J. L. Rousset, F. J. Cadete Santos Aires, B. R. Sekhar, P. Melinon, B Prevel, M. Pellarin, *J. Phys. Chem. B* **2000**, *104*, 5430.

134. W. C. Li, M. Comotti, F. Schüth, *J. Catal.* **2006**, *237*, 190.

135. A. Wang, Y. P. Hsieh, Y. F. Chen, C. Y. Mou, *J. Catal.* **2006**, *237*, 197.

136. A. B. Hungria, N. D. Browning, R. P. Erni, M. Fernandez-Garcia, J. C. Conessa, J. A. Perz-Omil, A. Matinez-Arias, *J. Catal.* **2005**, *235*, 251.

137. K. Sun, J. Liu, N. K. Nag, N. D. Browning, *J. Phys. Chem. B* **2002**, *106*, 12239.

138. S. Storsaeter, B. Totdal, J. C. Walmsley, B. S. Tanem, A. Holmen, *J. Catal.* **2005**, *236*, 139.

139. P. W. Selwood, *Chemisorption and Magnetization*, Academic Press, New York, 1975, 172 pp.

140. J. A. Dalmon, in *Catalyst Characterization: Physical Techniques for Solid Materials*, B. Imelik, J. C. Védrine (Eds.), Plenum Press, New York, 1994, Chapter 21, pp. 585–609.

141. A. Barbier, A. Hanif, J. A. Dalmon, G. A. Martin, *Appl. Catal. A* **1998**, *168*, 333.

142. J. Llorca, J. A. Dalmon, P. Ramirez de la Piscina, N. Homs, *Appl. Catal. A* **2003**, *243*, 261.